Easterly Waves in the East Pacific during the OTREC 2019 Field Campaign

LIDIA HUAMAN,[a] ERIC D. MALONEY,[b] COURTNEY SCHUMACHER,[a] AND GEORGE N. KILADIS[c]

[a]*Department of Atmospheric Sciences, Texas A&M University, College Station, Texas*
[b]*Department of Atmospheric Science, Colorado State University, Fort Collins, Colorado*
[c]*Physical Sciences Division, NOAA/Earth System Research Laboratory, Boulder, Colorado*

(Manuscript received 6 May 2021, in final form 6 August 2021)

ABSTRACT: Easterly waves (EWs) are off-equatorial tropical synoptic disturbances with a westward phase speed between 11 and 14 m s^{-1}. Over the east Pacific in boreal summer, the combination of EWs and other synoptic disturbances, plus local mechanisms associated with sea surface temperature (SST) gradients, define the climatological structure of the intertropical convergence zone (ITCZ). The east Pacific ITCZ has both deep and shallow convection that is linked to deep and shallow meridional circulations, respectively. The deep convection is located around 9°N over warm SSTs. The shallow convection is located around 6°N and is driven by the meridional SST gradient south of the ITCZ. This study aims to document the interaction between east Pacific EWs and the deep and shallow meridional circulations during the Organization of Tropical East Pacific Convection (OTREC) field campaign in 2019 using field campaign observations, ERA5, and satellite precipitation. We identified three EWs during the OTREC period using precipitation and dynamical fields. Composite analysis shows that the convectively active part of the EW enhances ITCZ deep convection and is associated with an export of column-integrated moist static energy (MSE) by vertical advection. The subsequent convectively suppressed, anticyclonic part of the EW produces an increase of moisture and column-integrated MSE by horizontal advection that likely enhances shallow convection and the shallow overturning flow at 850 hPa over the southern part of the ITCZ. Therefore, EWs appear to strongly modulate shallow and deep circulations in the east Pacific ITCZ.

KEYWORDS: Intertropical convergence zone; Pacific Ocean; Meridional overturning circulation; Synoptic-scale processes

1. Introduction

Easterly waves (EWs) are prominent synoptic (i.e., 2–10-day period) features in the Pacific intertropical convergence zone (ITCZ) with westward phase speeds between 11 and 14 m s^{-1} (Serra et al. 2008). EWs commonly serve as precursors to tropical cyclones and hurricanes in the east Pacific (Pasch et al. 2009; Serra et al. 2010) and are associated with 25%–40% of the deep convective clouds and produce up to 50% of the seasonal precipitation over the far east Pacific during boreal summer (Dominguez et al. 2020). Thus, EWs impact both the weather and climate of the east Pacific ITCZ.

EWs are found in the eastern Atlantic and West Africa (Reed et al. 1977; Kiladis et al. 2006; Berry et al. 2007; Janiga and Thorncroft 2013; Gomes et al. 2019), east Pacific (Tai and Ogura 1987; Raymond et al. 1998; Zehnder et al. 1999; Serra et al. 2008; Rydbeck et al. 2017), the western and central Pacific (Reed and Recker 1971; Reed and Johnson 1974), and the Caribbean Sea (Riehl 1954). In the east Pacific, EWs are consistent with Riehl's classical "inverted trough" model (Riehl 1954). In this model, positive specific humidity anomalies are concentrated in the lower troposphere in advance of the trough axis and deepen within and behind the trough where enhanced convection and column-integrated moisture anomalies are favored. The maximum vertical component of vorticity is located between 700 and 600 hPa and EW wavelengths range between 4200 and 5900 km. Ahead of the wave (i.e., west of the trough axis), the planetary boundary layer (PBL) is warm and moist, and northerly winds are predominant. Behind the wave (i.e., east of the trough axis), the PBL is cold and dry and dominated by southerly winds. Serra et al. (2010) showed that while some east Pacific EWs originate from Atlantic disturbances east of 70°W, others are generated locally in the Caribbean and east Pacific. Additionally, it is important to mention that the EWs predominate over warm sea surface temperature (SST) regions and notable mean meridional humidity gradients. Rydbeck and Maloney (2015) showed that anomalous meridional winds acting on the mean meridional moisture gradient of the ITCZ produce moisture anomalies that enhance convection in the though side of the EW. The orientation of EWs is generally southwest–northeast, which helps an EW maintain kinetic energy through barotropic conversion in the presence of a meridionally sheared zonal flow (Rydbeck and Maloney 2014; Rennick 1976; Thorncroft and Hoskins 1994).

EWs are important features of the east Pacific ITCZ. The net effect of many synoptic-scale disturbances, such as EWs and convectively coupled equatorial waves (CCEWs; Kiladis et al. 2009; Serra et al. 2014; Huaman et al. 2020), plus local mechanisms like low-level convergence produced by strong meridional SST gradients (Lindzen and Nigam 1987; Back and Bretherton 2009), define the climatological structure of the ITCZ. The mean vertical structure of the east Pacific ITCZ has been studied in some detail. Back and Bretherton (2006) showed maximum vertical

Supplemental information related to this paper is available at the Journals Online website: https://doi.org/10.1175/JAS-D-21-0128.s1.

Corresponding author: Lidia Huaman, lidiana.huaman@tamu.edu

DOI: 10.1175/JAS-D-21-0128.1

motion at 850 hPa based on reanalysis fields that was associated with an import of moist static energy (MSE) through vertical advection. However, a second vertical motion peak aloft was observed using two months of data from the East Pacific Investigation of Climate Processes in the Coupled Ocean–Atmosphere System (EPIC-2001) field campaign and satellite data (Zhang et al. 2004, 2008; Huaman and Takahashi 2016). Additionally, Huaman and Schumacher (2018) used 16 years of *CloudSat* and Tropical Rainfall Measuring Mission (TRMM) satellite data to demonstrate that two peaks of latent heating associated with deep and shallow convection are apparent in this region and linked to deep and shallow meridional circulations. They also found that the vertical structure of the ITCZ is tilted meridionally; shallow convection occurs around 6°N in the southern part of the ITCZ, and transitions to deep convection around 9°N in the northern part of the ITCZ.

Most of the studies in the east Pacific have relied on reanalyses to describe the three-dimensional structure of EWs. The lack of direct observations in the east Pacific causes reanalysis datasets to rely heavily on model physical parameterizations, supporting the need for targeted field campaigns. Serra and Houze (2002) used the Tropical Eastern Pacific Process Study (TEPPS-1997) research cruise dataset to study synoptic-scale convection and found that EWs are prominent convective features during boreal summer. Petersen et al. (2003) used the EPIC-2001 field campaign dataset to study EWs, revealing their thermodynamic characteristics and four-dimensional precipitation structure using shipborne C-band, Doppler radar data. The Organization of Tropical East Pacific Convection (OTREC) is the latest field campaign over the east Pacific and took place from 5 August to 3 October 2019 (Fuchs-Stone et al. 2020). OTREC goals were to determine the large-scale environmental factors that control convection over the tropical oceans and to characterize the interaction of convection with tropical disturbances, especially EWs. OTREC used the NSF/National Center for Atmospheric Research (NCAR) Gulfstream V aircraft to survey the east Pacific and deploy gridded patterns of dropsondes from a high altitude (i.e., 13 km) to characterize the large-scale environmental state and integrated effects of convection. The aircraft also provided profiles of radar reflectivity with a W-band radar.

Figure 1 shows the mean precipitation from the Integrated Multisatellite Retrievals for Global Precipitation Measurement (IMERG) dataset and mean SST from the Operational Sea Surface Temperature and Sea Ice Analysis (OSTIA) (Fig. 1a) and a cross section of vertical motion and flow in the meridional plane over the far east Pacific from ERA5 reanalysis (Fig. 1b) for August–September 2019, a period approximately corresponding to the OTREC field campaign period. Section 2 describes the precipitation and reanalysis datasets in more detail. The OTREC field campaign was held in the far east Pacific in a box delineated approximately by 0°–13°N, 89°–86°W (indicated by the blue rectangle in Fig. 1a); this will hereafter be called the OTREC region box. Over the OTREC region box the maximum precipitation (Fig. 1a) was located around 9°N over a weak SST gradient (i.e., the east Pacific warm pool) and precipitation extended toward this region from the Colombian coast (Toma and Webster 2010a,b). A strong meridional SST gradient was seen south of the precipitation maximum, with coldest SSTs south of the equator (i.e., the east Pacific cold tongue). The vertical motion cross section (Fig. 1b) shows shallow and deep vertical motion peaks associated with differing convective profiles that are linked to shallow and deep circulations, respectively. Jaramillo et al. (2017) showed that the deep convection located around 8°N over warmer SSTs is associated with mesoscale convective systems (MCSs), while the shallow vertical motion peak at 6°N has been shown to be driven by the strong SST meridional gradient and associated low-level convergence (Lindzen and Nigam 1987) that forms shallow cloud structures with light precipitation (Huaman and Schumacher 2018). The shallow structures likely do not evolve into deep structures because of the cooler SST and dry upper-level air in that region (Zuidema et al. 2006).

Most previous studies about the vertical structure of the east Pacific ITCZ and associated circulations have been focused on seasonal scales, but synoptic variations of the deep and shallow circulations have not yet been examined in detail. Further, previous analyses were limited to reanalysis data and satellite

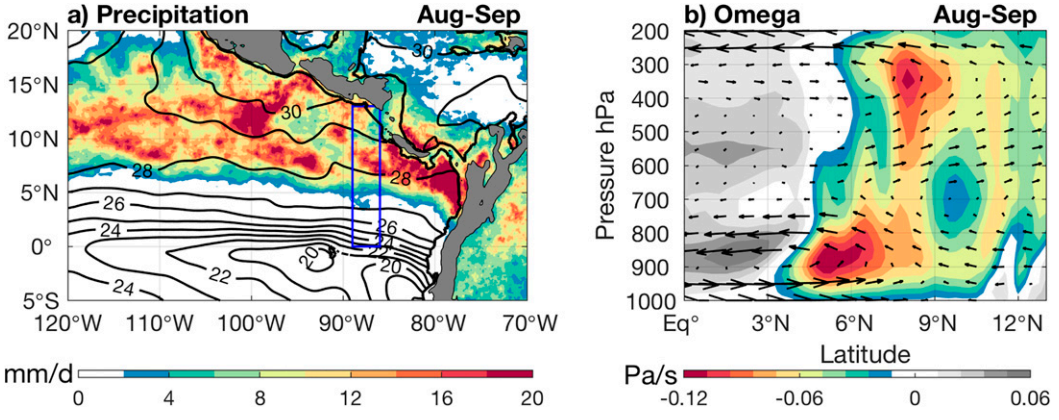

FIG. 1. (a) Total precipitation (mm day^{-1}) from IMERG and SST (°C) from OSTIA, and (b) cross section of omega (Pa s^{-1}) and meridional flow across the OTREC region [blue rectangle in (a)] from ERA5 for August and September 2019.

retrievals (e.g., Back and Bretherton 2006; Handlos and Back 2014; Huaman and Takahashi 2016; Huaman and Schumacher 2018) because of the lack of observations in the east Pacific. In this study, we aim to 1) characterize the synoptic variability in the east Pacific during the OTREC 2019 field campaign, providing useful large-scale context for more specialized studies in this region, and 2) understand how this synoptic variability influences convection and deep and shallow circulations in the east Pacific ITCZ during OTREC by modulating the moisture and MSE fields. The modulation of shallow and deep meridional circulations associated with the passage of EWs will be assessed using ERA5 fields, satellite precipitation, and OTREC field campaign data. Thompson et al. (1979) stated that shallow clouds were found to be abundant near the EW ridge, whereas detrainment from both deep and midlevel cumulus clouds dominated in the wave trough. We hypothesize that EWs alter the moisture and MSE fields that modify the strength of convection and the overturning circulation in the ITCZ region. This article is organized as follows: section 2 presents the data and methods. Section 3 describes the synoptic variability and the horizontal and vertical structure of EWs, followed by the moisture budget of the EWs in section 4. The interaction of EWs and the shallow and deep meridional circulations are presented in section 5, and a summary and conclusions are provided in section 6.

2. Data and methods

a. Data description

We used hourly data from ERA5 (Hersbach and Dee 2016) with a horizontal grid spacing of 0.25° and 37° pressure levels. The hourly ERA5 data were averaged to daily data. The variables from ERA5 used in this study include horizontal and vertical winds, specific humidity, temperature, and precipitation during the OTREC period (5 August–3 October 2019).

Daily precipitation retrievals from the Global Precipitation Measurement (GPM) mission (Hou et al. 2014) were also used. IMERG is a unified satellite precipitation dataset produced by NASA to estimate surface precipitation over most of the globe (Huffman et al. 2015). Precipitation estimates from the GPM core satellite are used to calibrate precipitation estimates from microwave and infrared sensors on other satellites. After merging the estimates from multiple satellites, surface precipitation maps are produced at 0.1° horizontal resolution in the IMERG product.

We also used OTREC dropsondes from the NSF/NCAR Gulfstream V aircraft. Flight operations for OTREC took place from 5 August to 3 October 2019. While other regions were also sampled, 12 research flights (RFs) were performed over an east Pacific OTREC flight box (3°–11°N, 89°–86°W), a slightly smaller area than the OTREC region delineated in Fig. 1a. Each flight lasted 6 h, starting in the southern part of the box at 1200 UTC and reaching the northern part at 1800 UTC. The flight pattern is shown in Fig. 1 of Fuchs-Stone et al. (2020). Around 32 dropsondes were deployed during each flight from an altitude near 13 km. The dropsondes collected measurements of horizontal winds, temperature, and humidity between the aircraft and the surface with vertical resolution of around 0.5 hPa. We downsampled the data to a resolution of 20 hPa. As part of the OTREC field campaign, radiosondes in Santa Cruz, Costa Rica (10.26°N, 85.58°W), were also launched between 20 August and 30 September 2019, at 0000 and 1200 UTC (1800 and 0600 local time, respectively). OTREC dropsonde and sounding data were sent to the Global Telecommunication System (GTS) and ERA5 assimilated these data.

In addition to dropsondes, we utilized observations from the High-performance Instrumented Airborne Platform for Environmental Research (HIAPER) Cloud Radar (HCR) installed on the NSF/NCAR Gulfstream V aircraft (Rauber et al. 2017). HCR is a polarimetric, millimeter-wavelength (W-band) radar that can detect light rain and ice and liquid clouds. It collects reflectivity and Doppler radial velocity measurements, which at a vertical incident angle include the vertical wind speed and particle fall speed. The aircraft flies at an average ground speed of 190 m s^{-1}, with a radar sampling rate of 0.1 s. All OTREC datasets were processed by NCAR (Vömel et al. 2021).

Additionally, *Geostationary Operational Environmental Satellite 16* (*GOES-16*) images were used to complement the OTREC dataset. *GOES-16* is a current geostationary satellite operated by NOAA and NASA and provides 16 spectral bands including 10 infrared (IR) channels. This study used the *GOES-16* longwave IR channel 14 with a 6 km × 6 km resolution processed by NCAR/EOL and available at http://catalog.eol.ucar.edu/maps/otrec.

b. Identification of EWs

The ERA5 and IMERG anomaly values used in the identification of the EWs were calculated by removing the first three harmonics of the seasonal cycle based on the climatology between 1998 and 2018. Additionally, the OTREC period average was removed in order to eliminate any decadal or interannual signal that may have occurred during this period. EWs during the OTREC campaign were identified as follows. First, precipitation anomalies and dynamical fields were filtered using a fast Fourier technique retaining wavenumbers between −20 and 0 and periods between 2.5 and 10 days corresponding to EWs. This filtered domain band is also referred to as tropical depression (TD) type disturbance region (Frank and Roundy 2006). Although this region of wavenumber–frequency space includes both TD-type disturbances and mixed Rossby–gravity (MRG) waves (Yokoyama and Takayabu 2012), we are confident that the features we derived are EWs since the horizontal structure of winds and vorticity for each event are also consistent with previous EW studies. Additionally, we used an extended time period for this calculation (from June to November 2019) to minimize edge effects and ensure no data loss due to filtering for the OTREC period.

We calculated the total precipitation and TD-band precipitation anomaly averaged over the OTREC flight box (3°–11°N, 89°–86°W) and identified potential convectively active EW events when the total precipitation and TD-band precipitation anomaly were larger than the mean + 1.25 standard deviation. While we begin our identification of EWs with strong filtered precipitation signals in the east Pacific ITCZ, the potential EWs defined on the basis of precipitation were checked to ensure

they were also accompanied by strong filtered vorticity and meridional wind signals at 600 and 700 hPa that resemble EWs and not other westward-propagating disturbances such as MRG waves that have a similar phase speed but a different dynamical horizontal structure. In particular, the convectively active EWs selected had horizontal structures similar to those studied by Serra et al. (2008) and Rydbeck and Maloney (2015). Additionally, we ensured that the wave life cycle lasted more than 2 days as in Hodges (1995, 1999).

Figure 2 shows Hovmöller diagrams of total and EW filtered anomalies for precipitation, 600-hPa vorticity, and 600-hPa meridional wind in the OTREC flight box. The 700-hPa Hovmöller diagrams look generally similar to the 600-hPa Hovmöller, and are not shown. Based on the criteria discussed above, we identified three convectively active EWs in the Hovmöller precipitation diagram accompanied by strong vorticity and meridional wind signals that propagated from southwest to northwest. EWs 1 and 3 produced enhanced precipitation in the OTREC region on 7 August and 17 September, respectively, associated with positive vorticity anomalies at 600 hPa. Southerly wind anomalies at 600 hPa were seen the next day. EW 2 produced enhanced precipitation in the OTREC region on 15 August, and the strongest vorticity and southerly wind anomalies were seen at 700 hPa (not shown). EWs 1 and 2 showed strong signals of precipitation over the Caribbean (80°W) at day −1 and seemed to pass from the Caribbean to the east Pacific (90°W), although EW 3 appeared to be generated in the east Pacific (not shown). Although vorticity and meridional winds displayed westward propagation during the last two weeks of September, these propagating features did not have a strong reflection in precipitation, and hence are not analyzed further here.

The total precipitation and TD-band precipitation anomaly time series over the OTREC flight box are shown in Fig. 3. The convectively active EWs identified had a strong positive precipitation peak (>17 mm day^{-1}), accompanied by cyclonic vorticity anomalies as seen in Fig. 2, followed by suppressed precipitation two days later. There were two additional events that exceeded our 1.25 deviation standard threshold but, based on Fig. 2, were not analyzed further due to the lack of vorticity and meridional wind signals (9 September) or unclear precipitation propagation (25 September). Two OTREC RFs coincided with the passage of the EWs we identified. The first OTREC RF, on 7 August, corresponded to a day with enhanced precipitation associated with the trough of the EW. The other OTREC RF, on 17 August, corresponded to a day with suppressed precipitation associated with the ridge of the EW. Although OTREC RFs only partially captured two EWs, ERA5 data were employed to study the three EWs previously identified with the IMERG data. ERA5 assimilated all available dropsondes and intensive radiosonde operations occurred in Costa Rica and Colombia during OTREC that provided further constraints on the reanalysis fields for all EWs examined.

3. Horizontal and vertical structure of the OTREC EWs

a. Composite EW structure

Figures 4 and 5 show the composite precipitation during the passage of the three EWs. Precipitation at day 0 (Figs. 4a and 5c)

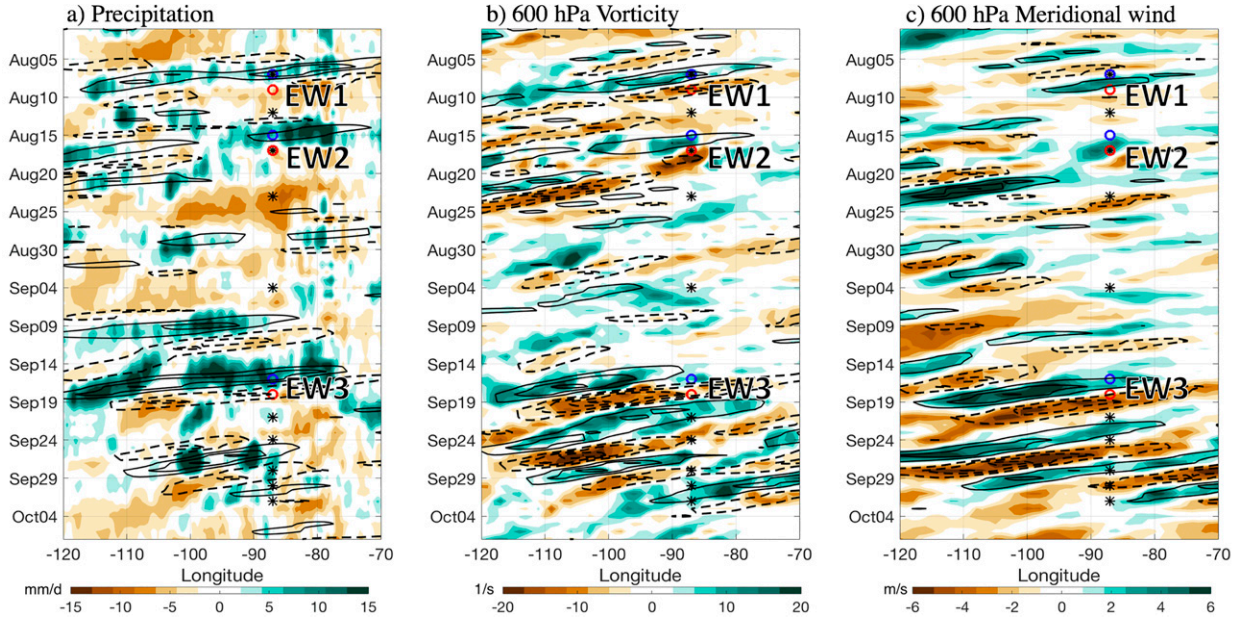

FIG. 2. Hovmöller diagrams averaged from 3° to 11°N of (a) precipitation (mm day^{-1}) from IMERG, and (b) 600-hPa vorticity (s^{-1}) and (c) 600-hPa meridional winds (m s^{-1}) from ERA5. Total values are shaded and TD-band values are in contours (precipitation contours every 4 mm day^{-1}, vorticity contours every 4 s^{-1}, and 600-hPa meridional wind contours every 2 m s^{-1}). Symbols are placed in the OTREC region, the stars indicate OTREC RF dates, and the circles highlight enhanced convection (blue) and suppressed convection (red) associated with EWs.

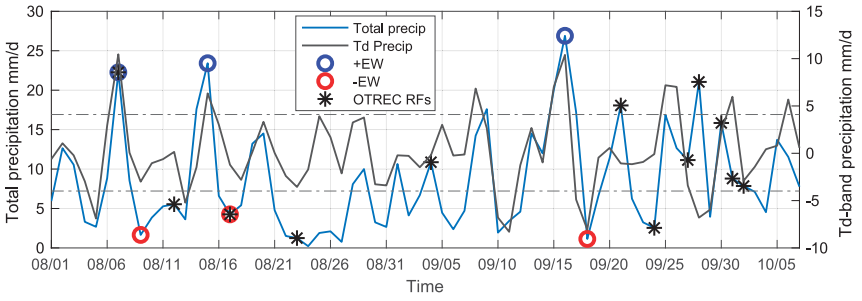

FIG. 3. Time series of total (left axis) and TD-band (right axis) IMERG precipitation over the east Pacific OTREC flight box (3°–11°N, 89°–86°W). Dashed lines indicates the threshold of TD-band precipitation over the OTREC period average ± 1.25 standard deviation. As in Fig. 2, the stars indicate OTREC RFs and the circles highlight when EWs were present.

corresponds to the precipitation averaged on 7 August, 15 August, and 17 September, when precipitation peaks in the OTREC region, and day +2 (Figs. 4b and 5h) represents the suppressed precipitation phase two days later. On day 0, enhanced precipitation associated with the convective part of the EW was seen over the far east Pacific ITCZ centered over the OTREC box. At day +2, the enhanced precipitation associated with the EW propagated northwestward along the coast to 17°N, 105°W, while precipitation became suppressed in the OTREC box. The intense precipitation at 10°N, 100°W is caused by the EW and the northwestward propagation is confirmed in Fig. 5. The mean zonal phase speed of the three EWs was estimated from the longitude–time diagram of composite precipitation for the latitude range 3°–11°N, which corresponds to the OTREC flight box latitudes (Fig. 4c). Composite precipitation associated with the EWs propagated westward at about 11.5 m s^{-1} between 80° and 115°W, although it was slower near 100°W. The zonal propagation of precipitation was seen both in the total precipitation (Fig. 4c) and precipitation anomalies (Fig. 4d), although it should be noted that there was also substantial meridional propagation (not shown).

Figure 5 shows the composite horizontal structure of EW precipitation anomalies and 600-hPa horizontal wind anomalies and the north–south cross sections of vertical velocity and meridional motion in the OTREC box from day −2 to day +3. We used vertical velocity as a proxy for convective strength. Weak vertical motion (i.e., vertical velocities between −0.05 and 0.05 Pa s^{-1}) were seen at 9°N, 90°W, especially at low levels (below 600 hPa) due to the cold SSTs in this region (i.e., the Costa Rica dome; Xie et al. 2005) that inhibit deep convection. At day −2 (Figs. 5a,d), positive precipitation anomalies of about 10 mm day^{-1} were located in the ITCZ axis, with generally easterly 600-hPa wind anomalies. Over the OTREC box, the vertical motion cross section suggests shallow and deep convection similar to the August–September average cross section in

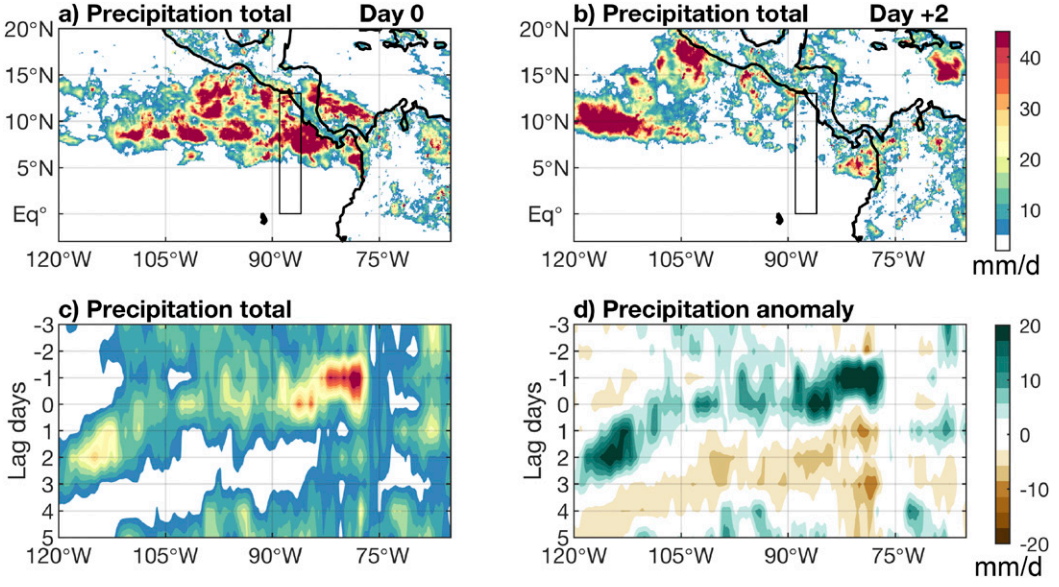

FIG. 4. IMERG precipitation (mm day^{-1}) averaged over the three OTREC EWs during (a) enhanced (day 0) and (b) suppressed (day +2) conditions. Longitude–time diagrams of (c) total precipitation and (d) anomaly precipitation for the latitude range 3°–11°N during the three EW events. The black box indicates the OTREC region box.

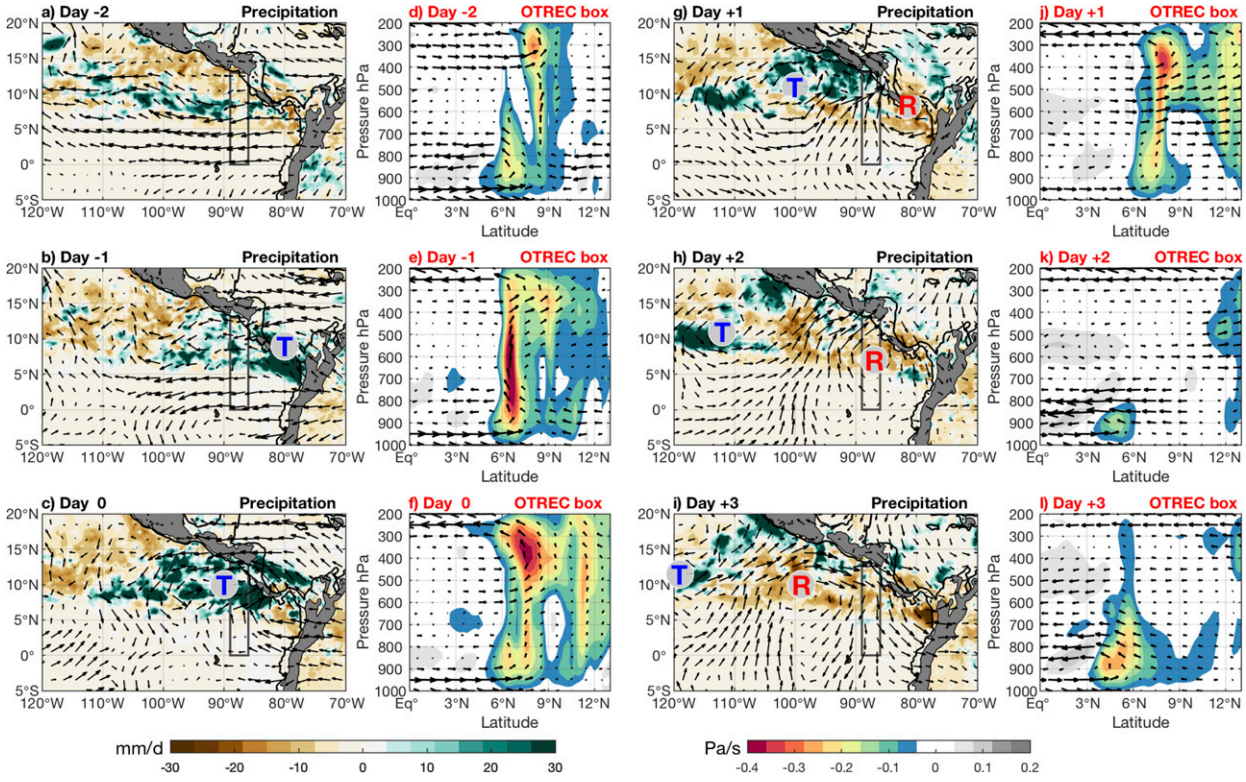

FIG. 5. (a)–(c),(g)–(i) Precipitation anomalies (mm day^{-1}) superimposed with 600-hPa horizontal wind anomalies across the east Pacific and (d)–(f),(i)–(l) omega cross sections (Pa s^{-1}) superposed by meridional flow over the OTREC region (gray rectangle) from day −2 to day +3 composited for the three EWs. The trough and ridge centers of the EW are labeled as T and R, respectively. Largest wind vector is 5 m s^{-1}.

Fig. 1b. Shallow convection associated with a shallow meridional circulation was located at 850 hPa and 6°N, while deep convective vertical motion associated with a deep meridional circulation was located at 300 hPa and 8°N.

At day −1 (Figs. 5b,e), enhanced precipitation (with anomalies larger than 30 mm day^{-1}) associated with the EW trough (i.e., the center of maximum vorticity) was greatest at 80°W, slightly east of the OTREC box. Over the OTREC box, ahead of the EW trough, the northerly flow at 850 hPa associated with the shallow circulation weakened from 4 m s^{-1} at day −2 to 2 m s^{-1} at day −1 and the region of shallow vertical motion moved northward toward the region of deep convection. The trough of the EW was associated with a transition of the shallow convection structure over the OTREC box to a deep convective structure. Additionally, the anomalous wind field at 600 hPa indicated a strengthening of the Caribbean low-level jet (CLLJ) during the passage of EWs with easterly zonal wind anomalies around 5 m s^{-1} located near 15°N, 75°W that maximized at 925 hPa (not shown) and extended upward to 600 hPa (Martin and Schumacher 2011; Poveda et al. 2014; Rapp et al. 2014; Whitaker and Maloney 2018). The cyclonic circulation of EWs has been associated with strengthening of the CLLJ easterly flow at 850 hPa (Molinari and Vollaro 2000), which can then penetrate from the Caribbean into the Pacific through a gap in the mountains as the Papagayo jet (Shapiro 1986; Molinari et al. 1997). The variations of the CLLJ during OTREC are consistent with Whitaker and Maloney (2020), who showed the strengthening of the CLLJ and Papagayo jet during the passage of an individual EW in the east Pacific. However, further examination of the interactions between the CLLJ and EWs is outside the scope of this study.

At day 0 (Figs. 5c,f), the enhanced precipitation associated with the EW trough was located at 90°W, next to the OTREC box. The horizontal winds at 600 hPa were characterized by anomalous cyclonic rotation and positive midlevel vorticity that supported deep convection and enhanced precipitation. Raymond et al. (2014) used observational data over the tropics to show that midlevel vortices modify the virtual temperature profile (i.e., cooler below the midlevel vortex and warmer above) to create low-level instability that fosters strong low-level convergence and subsequent deep convection. Over the OTREC box, the deep circulation was dominant compared to the shallow circulation. The vertical velocity peak was centered at 400 hPa and 8°N, indicating a stratiform profile (Schumacher et al. 2004). A weak shallow vertical velocity peak also existed at day 0, consistent with the presence of updrafts in convective elements that accompany the stratiform features, as noted in previous studies (e.g., Masunaga and Luo 2016).

At day +1 (Figs. 5g,j), enhanced precipitation associated with the trough of the EW moved to 100°W, a few degrees west of the OTREC box, and the circulation field was oriented southwest–northeast. Over the OTREC box and behind

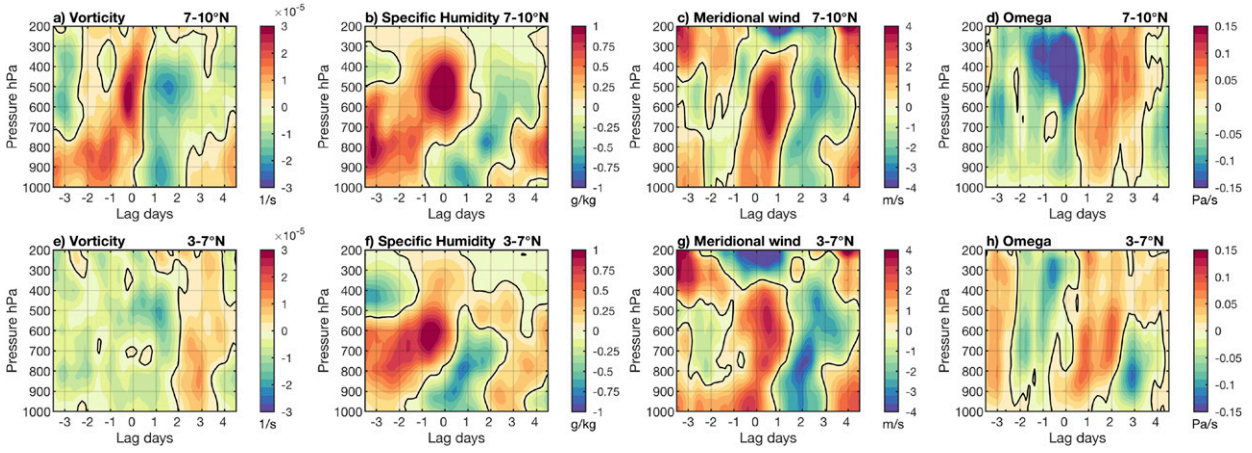

FIG. 6. Time–height diagrams of (left to right) vorticity (s^{-1}), specific humidity (g kg^{-1}), meridional wind (m s^{-1}), and omega (Pa s^{-1}) anomalies at (a)–(d) 7°–11°N and (e)–(h) 3°–7°N averaged at 89°–86°W over the three OTREC EWs.

the EW trough center, the vertical motion associated with deep convection was still strong but weaker compared to the previous day, and the shallow circulation was still muted. The deep convection was likely maintained by the enhanced midlevel southerly inflow associated with the cyclonic circulation of the EW that brings horizontal convergence (Huaman and Takahashi 2016; Nolan et al. 2007, 2010). At day +2 (Figs. 5h,k), the enhanced precipitation associated with the EW trough was centered at 15°N, 110°W, and suppressed precipitation and associated negative vorticity anomalies in the EW ridge (i.e., the center of minimum vorticity) were predominant over the OTREC box. The EW circulation was oriented west–east at day 0, but developed a southwest–northeast tilt on subsequent days. This tilted structure has been argued by previous studies to be associated with vortex stretching and horizontal elongation from southwest to northeast of the dynamical signature of the wave (Rydbeck and Maloney 2015). The cross section over the OTREC box shows suppressed deep convection and a pronounced shallow circulation with a strong overturning circulation at 850 hPa (i.e., meridional winds larger than 7 m s^{-1}) south of 6°N. This shallow circulation became deeper and strengthened at day +3 (Figs. 5i,l). The composite analysis suggests strong modification of the shallow and deep circulations during the passage of EWs, including intensification of the deep circulation at day +0 and shallow circulation at days +2 and +3. All three EWs examined during OTREC have qualitatively similar modulation of the deep and shallow circulations (Figs. S1–S3 in the online supplemental material). The mechanisms through which the deep and shallow circulations are modulated by the passage of the EWs will be discussed in section 5.

The vertical structure of EWs at the two latitude ranges where the deep and shallow circulations predominated will now be described. Figure 6 shows time–height diagrams of anomalous ERA5 vorticity, specific humidity, meridional wind, and vertical velocity composited for the three EWs over the northern part of the OTREC box (7°–11°N) where the deep circulation in the ITCZ was dominant (Figs. 6a–d) and the southern part of the OTREC box (3°–7°N) where the shallow circulation was dominant (Figs. 6e–h). We note that the composite evolution of the EW vertical structure during the OTREC campaign in the northern part of the ITCZ is consistent with Serra et al. (2008).

At days −2 and −1, ahead of the EW trough, positive vorticity (Fig. 6a), positive humidity anomalies (Fig. 6b), and northerly winds (Fig. 6c) occurred below 600 hPa between 7° and 10°N, with upward vertical motion anomalies throughout the troposphere (Fig. 6d). However, the southern part of the OTREC box (3°–7°N) was not as strongly impacted by the EWs, and the vorticity (Fig. 6e) and upward motion (Fig. 6h) anomalies were weak. Northerly winds associated with the cyclonic circulation of the EW were not seen but instead southerly winds below 850 hPa (Fig. 6g) dominated over this region. At day 0, within the convective part of the EW, positive vorticity and strong upward vertical velocity anomalies occurred throughout the troposphere between 7° and 10°N, with positive specific humidity anomalies above 800 hPa and negative specific humidity anomalies below 800 hPa. The meridional wind anomalies suggest a strengthening of the deep meridional circulation, with intensification of the upper-level (200 hPa) meridional outflow and low to midlevel meridional inflow, especially around 600 hPa where anomalies were up to 5 m s^{-1}. This structure is consistent with convective and stratiform structures in MCSs with deep circulations (Whitaker and Maloney 2020) and in other equatorial disturbances (Kiladis et al. 2009). However, in the southern part of the OTREC box, the vorticity and upward vertical motion anomalies were weak throughout the troposphere at day 0, which suggests only weak impact of EWs on shallow convection and associated circulations at these latitudes. At day +2, behind the trough of the EW, negative vorticity anomalies and downward anomalous vertical motion were seen throughout the troposphere with anomalous northerly winds at midlevels between 7° and 10°N. In the southern part, positive vorticity anomalies and positive specific humidity anomalies occurred, with strong meridional outflow around 800 hPa characterized by anomalies up to 4 m s^{-1} and shallow upward vertical motion that intensified until day +3, suggesting significant impacts on shallow

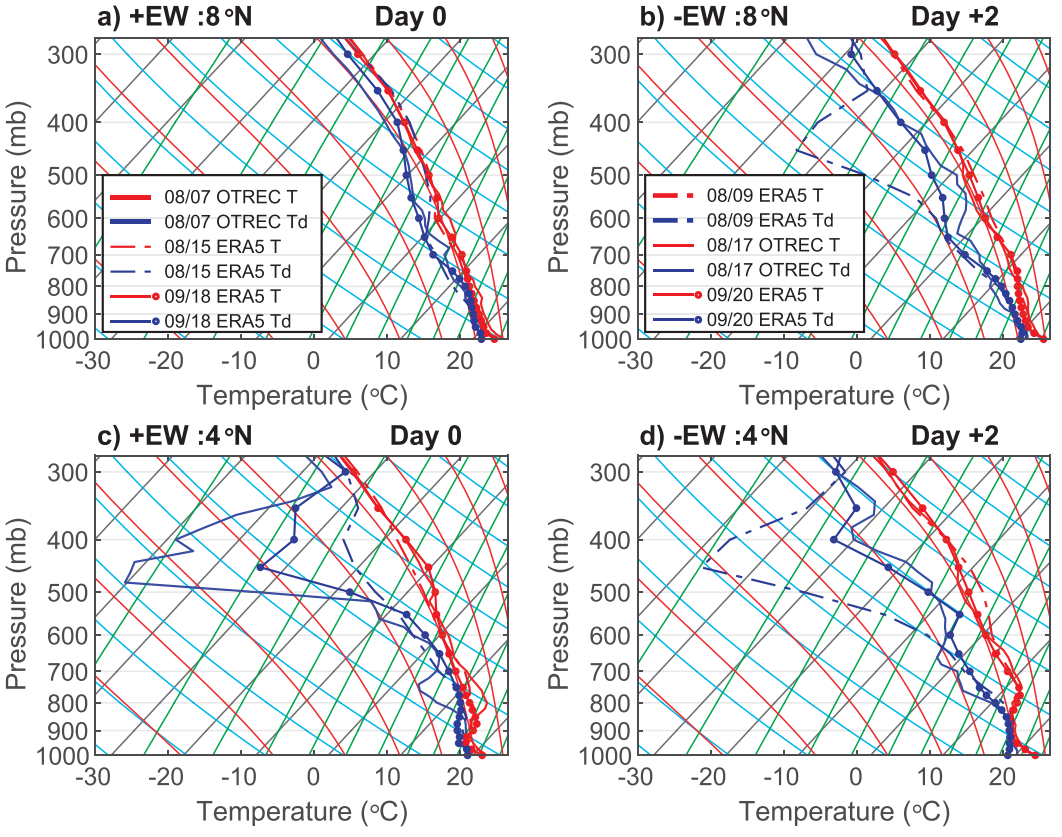

FIG. 7. Skew T diagrams for all the three EWs (7 Aug, 15 Aug, and 18 Sep) during the OTREC field campaign from ERA5 and OTREC RFs at (left) day 0 and (right) day 2 for (a),(b) 8°N and (c),(d) 4°N. RF times are between 1200 and 1800 UTC.

convection and associated circulations at these latitudes. The vertical structure of the EWs between 7° and 10°N from ERA5 was consistent with the vertical structure of EW 3 derived using OTREC radiosondes from Santa Cruz (not shown).

b. *Individual EWs*

We now analyze the individual EW events using the OTREC field campaign observations, supplemented by ERA5 and GOES IR imagery. Two RFs occurred during the passage of EWs (Figs. 2 and 3). During OTREC RF 1 (7 August), the NSF/NCAR Gulfstream V aircraft flew in the region of enhanced precipitation associated with the trough of EW 1. During OTREC RF 5 (17 August), the aircraft flew in the suppressed precipitation associated with the ridge of EW 2.

Figure 7 shows the air temperature (red) and dewpoint temperature (blue) profiles at days 0 and +2 at 8° and 4°N during all three EWs from ERA5 and OTREC. We used OTREC dropsondes from two RFs and used profiles from ERA5 for the other times. ERA5 profiles are similar to the OTREC profiles during the 7 and 17 August events shown here (Fig. S4). Table 1 shows the lifting condensation level

TABLE 1. LCL (hPa), CAPE (J kg^{-1}), and CIN (J kg^{-1}) at 4° and 8°N from the three EWs at days +0 and +2 from OTREC RFs and ERA5.

	Day 0					Day +2				
EWs	Source (date)	Lat	LCL	CAPE	CIN	Source (date)	Lat	LCL	CAPE	CIN
EW 1	OTREC (7 Aug)	8°N	971	1934	0	ERA5 (9 Aug)	8°N	958	1713	0
		4°N	977	395	−68		4°N	954	276	−30
EW 2	ERA5 (15 Aug)	8°N	968	1190	0	OTREC (17 Aug)	8°N	975	2259	0
		4°N	958	207	−46		4°N	975	1053	−12
EW 3	ERA5 (16 Sep)	8°N	974	1182	0	ERA5 (18 Sep)	8°N	956	1331	0
		4°N	972	62	−36		4°N	947	303	−44

(LCL), convective available potential energy (CAPE), and convective inhibition (CIN) values for each day and latitude.

At day 0 and 8°N (Fig. 7a), the soundings showed moist conditions throughout the troposphere associated with the convectively active part of the EWs (Figs. 5c,f). Table 1 indicates that the LCL was around 970 hPa in each EW, CAPE was 1934 J kg^{-1} for EW 1 and around 1185 J kg^{-1} for the other two EWs, while CIN was 0 J kg^{-1} for all EWs. At day +2 (Fig. 7b), when the composite EW trough had moved west and there was no longer a deep meridional circulation (Figs. 5h,k), a shallow moist layer was seen between 1000 and 900 hPa, with drier conditions above, especially during EW 1. The LCL varied between 956 and 975 hPa, making the LCL slightly higher in two of the three EWs (i.e., EW 1 and EW 3) at day +2 compared to day 0. CAPE increased in EW 2 and EW 3 at day 2, reaching 2260 J kg^{-1} in EW 2. This large value indicates that this index is inadequate by itself for detecting the potential for deep convection, as found in other studies (e.g., Sherwood et al. 2004), since suppressed convection is associated with the ridge of the EW (Fig. 5h). CIN remained zero in all three EWs at day +2.

At day 0 and 4°N (Fig. 7c), which represented conditions south of the main precipitation area of the convectively active EW, there was a layer of moist air below 800 hPa, consistent with shallow convection driven by the strong meridional SST gradients (Back and Bretherton 2009). Dry air predominated aloft, especially between 500 and 300 hPa. The temperature profiles also suggested a weak trade wind inversion between 950 and 850 hPa. Table 1 shows that the LCLs were similar to 8°N values but that CAPE was substantially less, with values ranging from 62 to 395 J kg^{-1}. CIN was strongly negative with values ranging from −36 to −68 J kg^{-1}. The decrease in CAPE and change to negative CIN can be explained by the large north-to-south variation in SST and vertical motion in the east Pacific ITCZ that substantially alters the boundary layer properties and impacts CAPE and CIN (e.g., Ye et al. 1998), such as the existence of the trade wind inversion at 4°N. At day +2 (Fig. 7d), the low-level moist layer extended up to 800 hPa and was capped by a stronger, deeper (between 850 and 750 hPa) inversion than on day 0. Conditions remained dry aloft. LCL heights became higher in EW 1 and EW 3 and CAPE increased in EW 2 and EW 3 (similar to the day 0 to day +2 trends at 8°N). CIN was less strongly negative compared to day 0 except in EW 3.

Figure 7 and Table 1 indicate that the thermodynamic structure variations of the three EWs between days 0 and +2 were qualitatively similar, although the magnitude of the variations showed substantial differences across events. Of note is a larger spread in the dewpoint profiles at the mid- and upper levels than in the temperature profiles, and this difference became more pronounced at 4°N. While it could be argued that some of this variability was introduced by only assimilating OTREC dropsondes in a subset of the profiles, the very strong dry air layer during EW 1 exists in the ERA5 profiles two days after the OTREC dropsondes were assimilated so it appears that the ERA5 can successfully represent EW structure and its variability to some extent. OTREC dropsondes launched through cloudy versus clear air may also account for some of this difference.

We now examine the convective structures seen by the HCR, the cloud radar installed on the NSF/NCAR Gulfstream V aircraft. On 7 August, RF 1 sampled a large MCS located in the northern part of the OTREC box (Fig. 8a). In regions of deep convective structures and stratiform rain regions with a well-defined bright band near an altitude of 4.5 km (Fig. 8c), the radar was strongly attenuated in the lower troposphere given the nature of W-band retrievals in deep convective systems. The southern part of the OTREC box did not show deep convection (Fig. 8b) and was impacted by very dry midlevel air (Fig. 7c). The HCR observed shallow cumulus clouds with echo-top heights around 1 km (or 900 hPa) and cirrus clouds near 10 km (Fig. 8d). On 17 August, RF 3 sampled suppressed convection in the northern part of the OTREC box associated with the nonconvective part of the EW that passed through 2 days before (Fig. 8e). The HCR detected

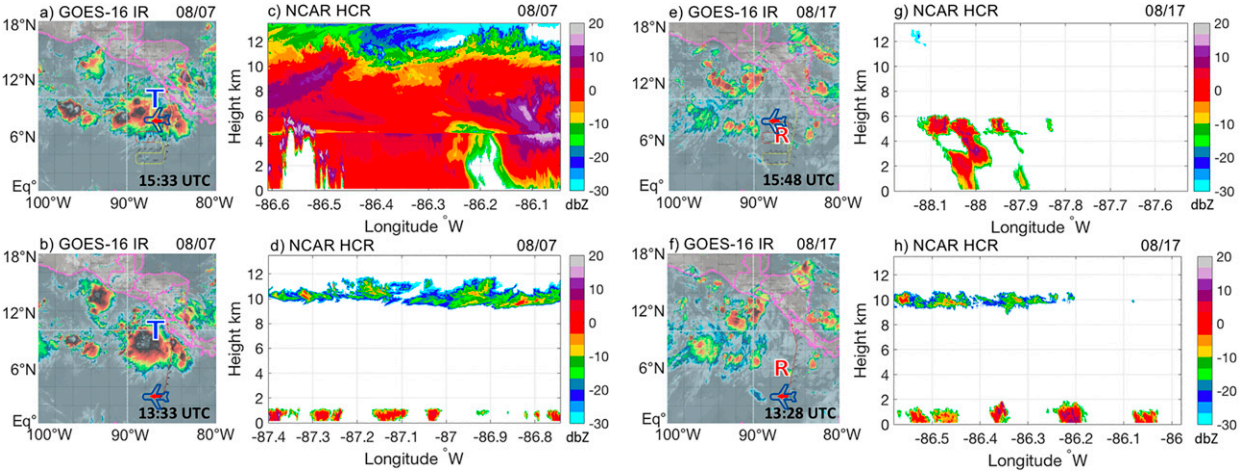

FIG. 8. (a),(b),(e),(f) GOES IR images (red/dark colors indicate convective regions) and (c),(d),(g),(h) vertical reflectivity cross sections (dBZ) from the NCAR HIAPER Cloud Radar during enhanced precipitation on 7 Aug 2019 (i.e., positive phase of EW) and suppressed precipitation on 17 Aug 2019 (i.e., negative phase of EW) across the flight path indicated by the red arrow in the GOES IR images. The trough and ridge centers of the EW are labeled as T and R, respectively.

isolated convective cells with echo-top heights near 6 km (Fig. 8g). In the southern part of the OTREC box (Fig. 8f), the HCR observed shallow cumulus clouds with echo-top heights at 1.5 km (or 850 hPa) and cirrus clouds at 10 km. The shallow cumulus extended slightly higher than those seen during RF1, potentially because of the elevated trade inversion at day +2 (cf. Figs. 7c,d). Therefore, deep convection in the northern part of the OTREC box and muted shallow convection in the southern part of the OTREC box dominated at day 0 when the trough center of the EW was near. Deep convection at day 0 was accompanied by an enhanced deep circulation (Fig. 5f). Suppressed deep convection in the northern part of the OTREC box and enhanced shallow convection in the southern part of the OTREC box dominated at day +2 with the EW ridge passage. The shallow convection at day +2 was accompanied by a strong shallow circulation (Fig. 5k). We performed a separate analysis with radar observations from the GPM satellite over the east Pacific OTREC box during the three EWs and also found stronger and deeper shallow structures in the southern part of the ITCZ at day +2 compared to day 0 (not shown).

4. Moisture budget

In this section, the moisture budget is examined to help understand why convection varies as a function of EW phase in climatologically shallow and deep regions. Many previous studies have shown that convection is favored when the lower free troposphere is moist (e.g., Raymond et al. 1998; Holloway and Neelin 2009). Rydbeck and Maloney (2015) further suggest that the distribution of convection within EWs is strongly constrained by the moisture field. The moisture budget is represented as

$$\left[\frac{\delta q}{\delta t}\right] = -[v_h \cdot \nabla_h q] - \left[\omega \frac{\delta q}{\delta p}\right] + E - P, \tag{1}$$

where q is specific humidity, v_h is horizontal wind, ω is vertical velocity, E is evaporation, and P is precipitation. The square brackets represent the mass-weighted vertical integral from 1000 to 200 hPa. The term on the left-hand side of Eq. (1) represents the vertically integrated specific humidity tendency. The first term on the right-hand side of Eq. (1) is the moisture tendency resulting from horizontal advection and the second term on the right-hand side is the moistening by vertical advection. These terms have been calculated using finite centered differences. The third and fourth terms on the right-hand side are the column moisture tendency as a result of surface evaporation and precipitation, respectively. In this study, we do not explicitly examine E because it was previously shown to be of second-order importance for determining the EW modulation of convection (Rydbeck and Maloney 2015). Vertical advection minus precipitation has parallels to the sum of vertical advection and radiation in the column-integrated MSE budget, and has been referred to as the "column process" by some studies (e.g., Wolding et al. 2016).

The vertically integrated moisture budget has been used to study regions with large precipitation produced by EWs. For example, Rydbeck and Maloney (2015) showed that anomalous horizontal advection has large contributions to the positive tendency of column-integrated moisture tendencies ahead of the EW convection, and to negative moisture tendencies behind the EW convection. Ahead of the cyclonic EW center, northeasterly flow advects moist air from the east Pacific warm pool, and behind the cyclonic EW center, southwesterly flow advects dry air from the east Pacific cold tongue. They also examined the difference between the tendency resulting from vertical advection and precipitation, calculated as the residual of the other terms in the budget to obtain the "column process." Positive regions of this quantity indicate where anomalous vertical advection is moistening the atmosphere more than anomalous drying by precipitation. Rydbeck and Maloney (2015) showed that while moistening not counteracted by precipitation preferentially occurs ahead of the wave trough, vertical advection minus precipitation is anomalously negative behind the wave trough. The difference between vertical advection and precipitation is substantially smaller than the total moisture tendency, suggesting that horizontal advection is the largest contributor to the positive tendency of column-integrated moisture tendencies ahead of EW convection.

This previous work implies in the context of the current study that shallow, nonprecipitating convection might play a moistening role ahead of the wave because of anomalously large low-level moisture convergence and suppressed precipitation. On the other hand, regions of stratiform rain from deep convection with muted low-level moisture convergence and large precipitation might play a drying role behind the wave. Figure 9 shows the composite moisture tendency anomalies resulting from horizontal advection and from vertical advection minus precipitation. We used precipitation from ERA5 in the moisture budget rather than IMERG because of the better physical consistency with the convergence field. The spatial structure of the ERA5 precipitation was generally consistent with the IMERG precipitation structure in Fig. 5; however, ERA5 precipitation anomalies were up to 20% lower within the EW at days −1, 0, and +1 (not shown).

At day −1 (Fig. 9a), the enhanced precipitation associated with the EW trough was located at 80°W and ERA5 precipitation (blue contours) showed a zonal band of precipitation at 8°N. While dynamical features resembling an EW at day −1 are generally weak, positive horizontal advection anomalies (shaded) were slightly less than 3 mm day^{-1} ahead of the wave (i.e., west of the trough axis) and around −5 mm day^{-1} behind the wave (i.e., east of the trough axis) near the South American coast. The difference between the vertical advection and precipitation (Fig. 9f) indicates anomalous moistening to the northwest (10°N, 83°W) of the convectively active part of the EW trough. At day 0 (Fig. 5c), enhanced precipitation was associated with the EW trough centered near 90°W, next to the OTREC box. Negative horizontal advection anomalies increased over the southeastern part of this convectively active region (Fig. 9b). The vertical advection and precipitation mostly cancel each other at the EW trough axis around 90°W, Fig. 9g), but moistening by vertical advection exceeded drying by precipitation ahead of the wave, suggesting a region with large low-level convergence and weak precipitation (i.e., cumulus congestus). Behind the wave, anomalous

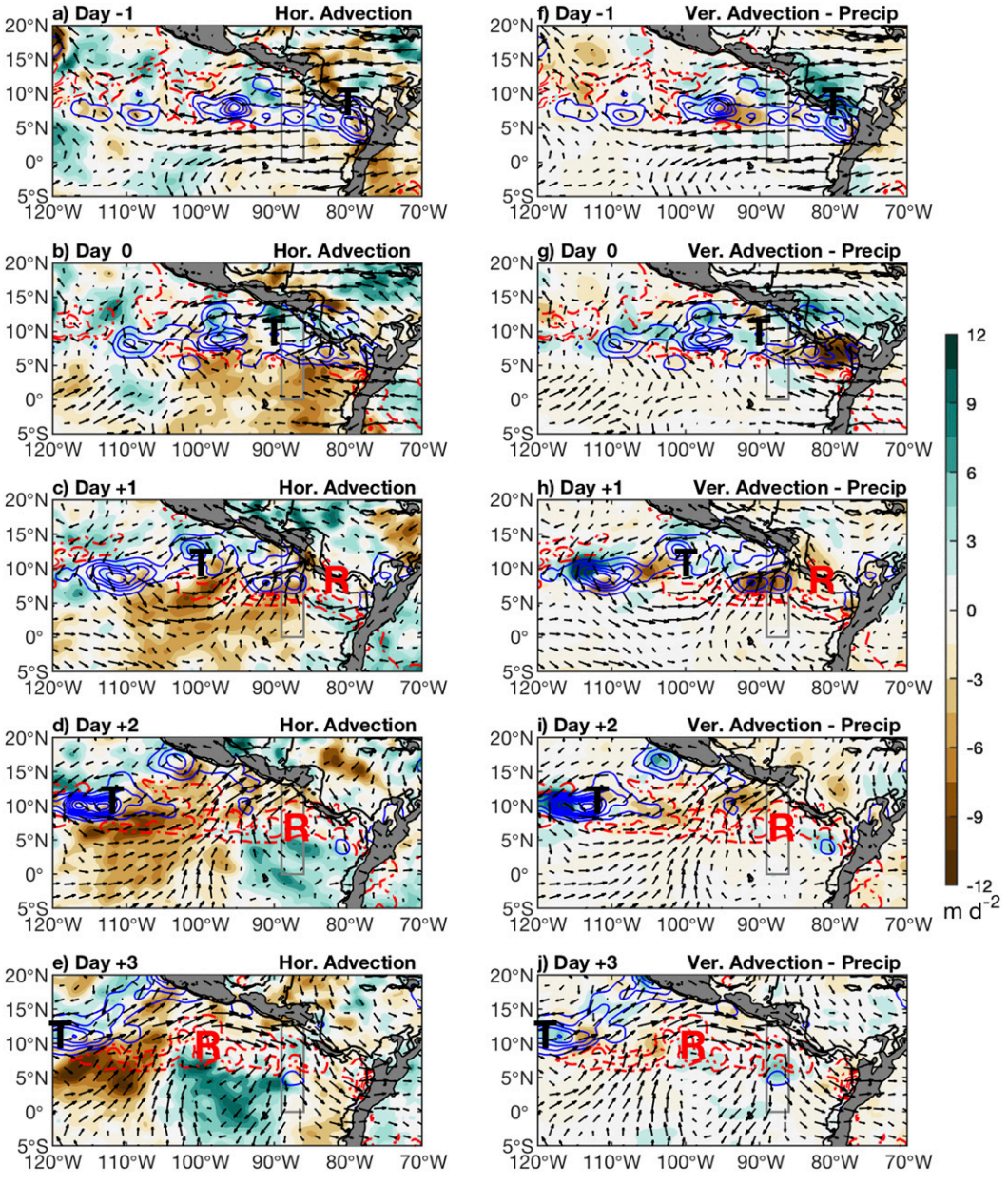

FIG. 9. Composite OTREC EW anomalies (shaded, mm day^{-1}) of (a)–(e) moisture tendency from horizontal advection and (f)–(h) moisture tendency from vertical advection minus precipitation from day −1 to day +3 using ERA5. All images are superposed by 600-hPa wind vectors and ERA5 precipitation anomalies. Positive (negative) precipitation anomalies are in blue (red) contours, contours are every 10 (5) mm day^{-1} starting at 5 mm day^{-1}. The trough and ridge centers of the EW are labeled as T and R, respectively. Largest wind vector is 5 m s^{-1}.

precipitation exceeded vertical advection, resulting in drying, suggesting a region with anomalously weak low-level convergence and enhanced precipitation (stratiform structures). These horizontal patterns, while noisier given the smaller sample size, are consistent with Rydbeck and Maloney (2015) and propagated westward in association with the EW.

At day +1 (Fig. 9c), enhanced circulation and precipitation associated with the EW trough were oriented southwest–northeast. The EW trough was centered at 100°W, with anomalous negative horizontal moisture advection behind the wave trough also oriented southwest–northeast. Over the OTREC box, anomalously negative horizontal moisture advection and 600-hPa southerly winds were predominant, consistent with intrusion of dry air from the equatorial region of the SST cold tongue. The difference between anomalous vertical advection and precipitation (Fig. 9h) suggests moistening by vertical advection exceeded drying by precipitation ahead of the wave. Behind the wave trough, precipitation

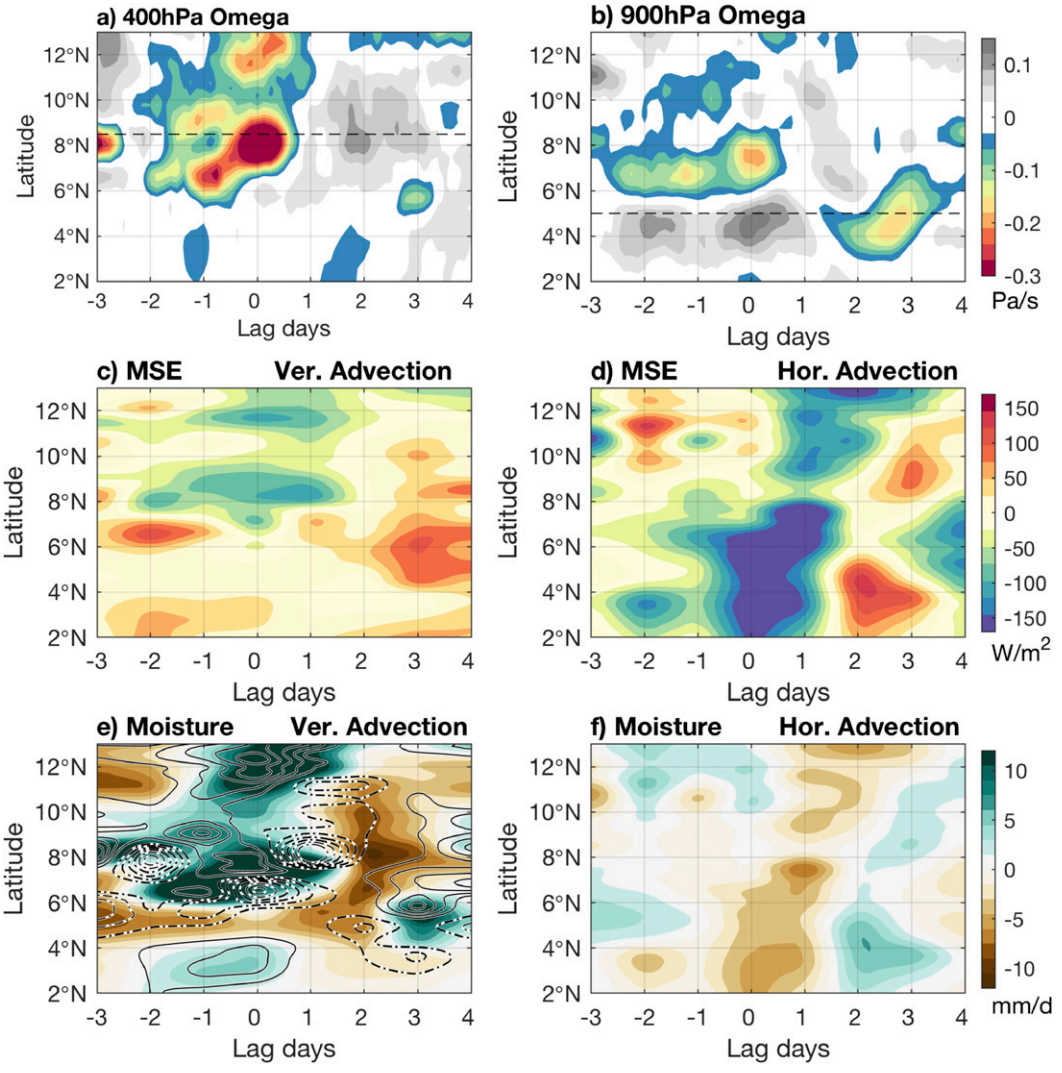

FIG. 10. Composite OTREC EW time–latitude diagrams over 89°–86°W of (a),(b) omega anomalies (Pa s^{-1}) at 400 and 900 hPa (dashed lines indicate the climatological position of maximum omega at the determined level), (c),(d) vertical and horizontal advection of total MSE (W m^{-2}), (e) anomalies of moisture tendency from vertical advection (mm day^{-1}) superposed by moisture tendency from vertical advection minus precipitation (mm day^{-1}; contours every 2 mm day^{-1}, negative values dashed and positive values solid), and (f) anomalies of moisture tendency from horizontal advection (mm day^{-1}).

exceeded vertical advection, resulting in drying. This behavior suggests shallow and stratiform structures ahead of and behind the wave trough, respectively. The stratiform structure behind the wave trough is consistent with Fig. 5j.

At days +2 and +3 (Figs. 9d,e), the convectively active part of the southwest–northeast oriented EW was centered around 110° and 115°W (i.e., the trough), respectively. As on the previous days, anomalous negative horizontal moisture advection was observed behind the wave. Over the OTREC box, the precipitation was suppressed. In the northern part of the OTREC box, anomalous negative horizontal moisture advection predominated, and in the southern part, anomalous positive horizontal moisture advection predominated. Since the EW was tilted with height, the time–height diagram in Fig. 6g can also be interpreted as longitude–height diagram. The horizontal flow was mainly northerly at 850 hPa in the southern part and this was the main source of moistening. The structure of the horizontal advection field likely played an important role in regulating local shallow convection and circulation near 4°–5°N (Figs. 5h–l and 8h). The difference between the vertical advection and precipitation (Figs. 9i,j) shows that moistening by vertical advection was small over the OTREC box at day +2 and positive around 5°N at day +3, also suggesting the importance of shallow convection there (Fig. 8h) for fostering column moistening in addition to horizontal advection.

Figures 10a and 10b show the EW composite time–latitude plots of omega at 400 and 900 hPa that display deep and

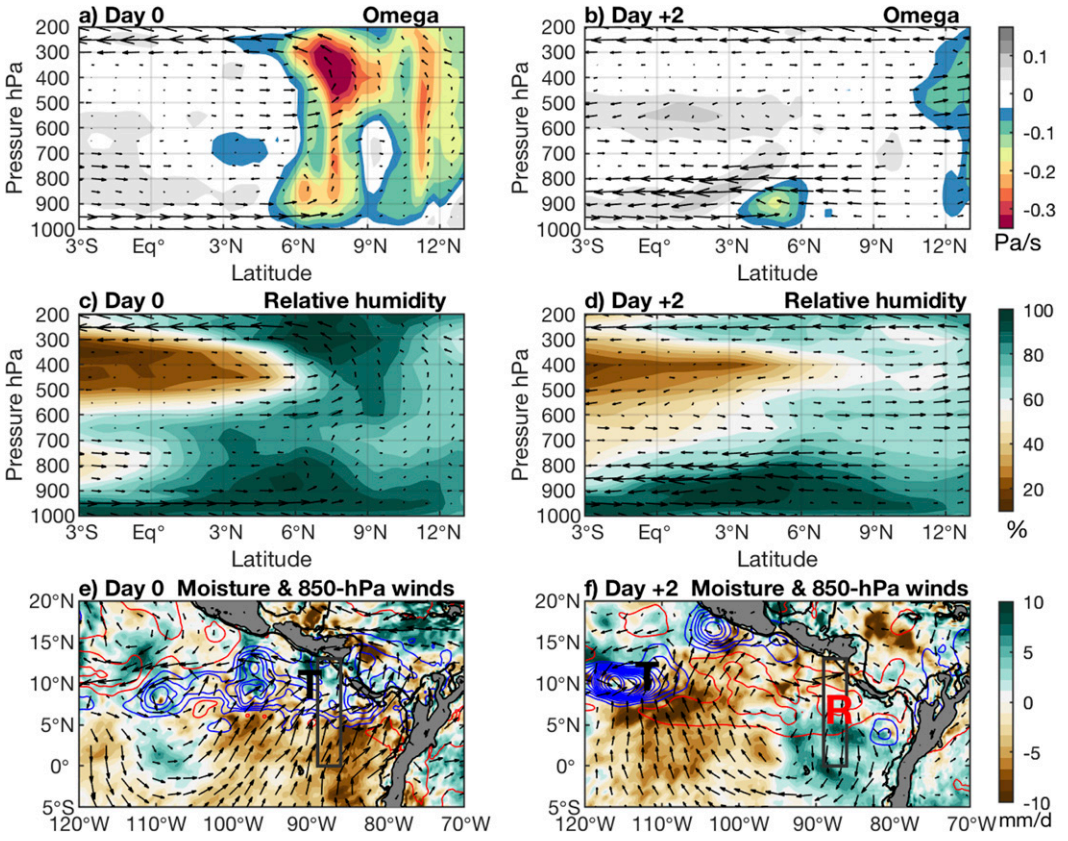

FIG. 11. Composite OTREC EW (a),(b) vertical velocity (Pa s^{-1}) and meridional flow, (c),(d) relative humidity (%) averaged over 89°–86°W, and (e),(f) anomalies of moisture tendency from horizontal advection (shaded) and vertical advection (contours) superposed by winds at 850 hPa during (left) day 0 and (right) day +2. Positive (negative) vertical advection anomalies are in blue (red) contours; contours are every 5 mm day^{-1} starting at 3 mm day^{-1}. The trough and ridge centers of the EW are labeled as T and R, respectively. Largest wind vector is 6 m s^{-1}.

shallow convective structure evolution, respectively. In the OTREC average (Fig. 1), omega peaks at 400 and 900 hPa were located at 8.5° and 5°N, respectively (dashed lines in Figs. 10a,b). The vertical and horizontal advection of MSE calculated as in Back and Bretherton (2006) are shown in Figs. 10c and 10d. MSE is a thermodynamic variable that helps explain the interactions between convection and the large-scale circulation. The MSE budget has an advantage over the moisture budget in the deep tropics where temperature gradients are weak in that it accounts for the cancellation of vertical moisture advection and drying by precipitation in the vertical advection term, especially when considered in conjunction with radiation (Wolding and Maloney 2015). Additionally, the vertical advection of MSE is strongly related to the shape of the vertical motion profile in the ITCZ, and its use provides direct comparison to studies involving the vertical structure of the ITCZ and moist static stability (Back and Bretherton 2006; Inoue and Back 2015). Positive values indicate an import of MSE and maximum vertical velocity at low levels (i.e., a bottom-heavy structure), and negative values indicate the export of MSE with maximum vertical velocity at high levels (i.e., a top-heavy structure). Additionally, the moisture tendency resulting from vertical and horizontal advection (section 4) are shown in Figs. 10e and 10f, respectively. Vertical advection minus precipitation is shown in contours in Fig. 10e.

For the deep convection regime at day 0 (Fig. 10a), the upper-level vertical velocity at 8°N is enhanced along with an anomalous export of MSE through vertical advection (Fig. 10c). The export of MSE suggests that precipitation was stronger than vertical moisture advection, consistent with Fig. 10e (contours). For the climatological shallow convection region near 4°–5°N, where the upward vertical motion is generally stronger at 900 hPa compared to 400 hPa, shallow convection was inhibited at day 0, especially at 4°N (Fig. 10b), with enhanced shallow convection at days +2 and +3 (cf. Figs. 5k–l). At day +2, the shallow convection region was characterized by an anomalous import of MSE (+100 W m^{-2}) and a positive moisture tendency resulting from horizontal advection (Figs. 10d,f) that would help support a deepening of the shallow clouds as suggested by the HCR data (Fig. 8h). The horizontal advection of MSE and the moisture tendency resulting from horizontal advection changed from negative values (<−150 W m^{-2} and −4 mm day^{-1}) at day 0 to positive values (+100 W m^{-1} and +3 mm day^{-1}) at days +2 and +3. It is interesting to note that although the strongest shallow meridional overturning occurred on day +2 (Fig. 5k), the largest low-

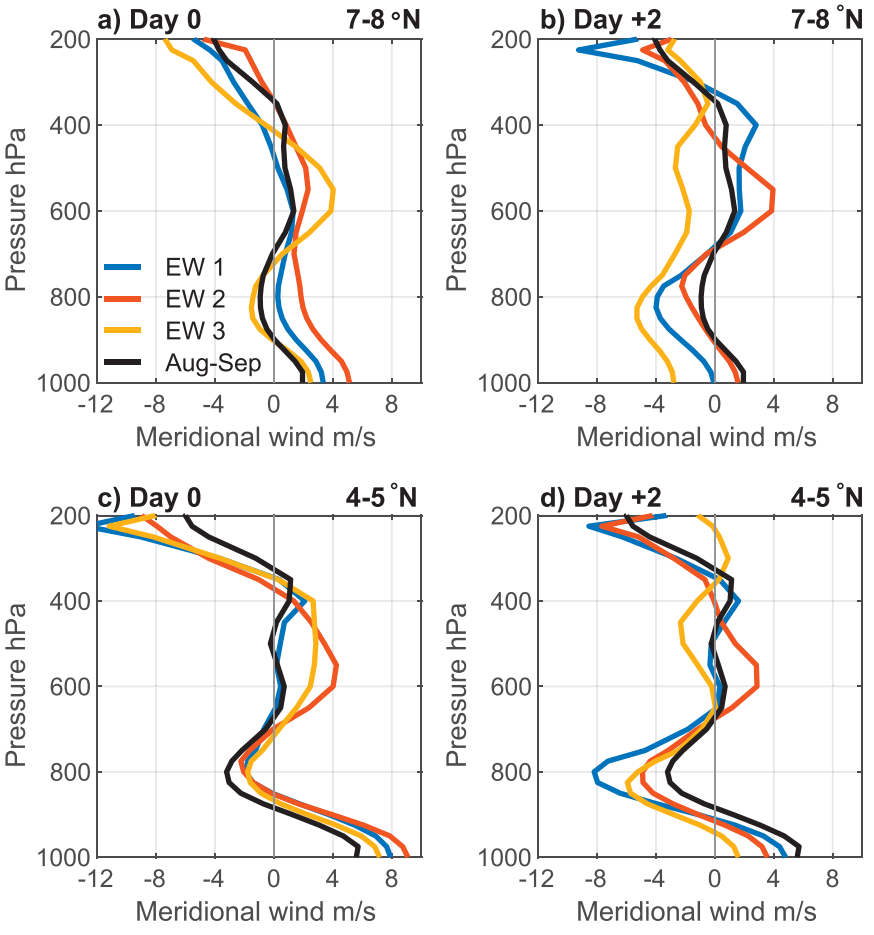

FIG. 12. Meridional wind profiles from ERA5 (m s^{-1}) at (a),(b) 7°–8°N, 89°–86°W and (c),(d) 4°–5°N, 89°–86°W for the three EWs and the August–September average during (a),(c) day 0 and (b),(d) day +2.

level vertical velocity occurred at day +3 (Fig. 5l). At day +3, the vertical moisture advection term was larger than the precipitation (Fig. 10e), consistent with the positive anomalous MSE import and indicative of the stronger congestus structures with large lower-tropospheric vertical velocity.

5. EWs and the shallow and deep meridional circulations

The horizontal and vertical structure of EWs and ensuing moisture tendency field changes suggest substantial perturbations to the climatological deep and shallow circulations during wave passage (Figs. 5, 8, and 9). In this section, we discuss mechanisms responsible for the modification of deep and shallow circulations during the passage of EW in more detail. Figures 11a–d show total vertical velocity and relative humidity cross sections during the enhanced (day 0) and suppressed (day +2) convection periods associated with the passage of EWs across the OTREC box.

At day 0, a deep circulation was observed in the ITCZ around 8°N with surface southerly inflow and return upper-level northerly outflow (Fig. 11a) and high relative humidity throughout the troposphere (Fig. 11c). The moisture tendency anomaly resulting from vertical advection was positive (8 mm day^{-1}) in this deep convection region (Fig. 11e). Dry inflow between 600 and 400 hPa (Figs. 7c and 11c) was also observed that could have induced a positive feedback to a deep convective structure by inducing temperature anomalies as proposed by Zuidema et al. (2006) and Nolan and Rappin (2008). However, in the southern part of the ITCZ, where a shallow circulation is found in the climatology (i.e., around 6°N), negative horizontal moisture and MSE advection anomalies were apparent inhibited shallow convection (Fig. 8d). The shallow circulation had a weak northerly overturning flow at 850 hPa between 3° and 6°N associated with the cyclonic circulation around the trough of the EW that provided southerly wind anomalies (Fig. 11e) and weakened the shallow circulation overturning flow (Fig. 11a).

At day +2, the deep circulation was muted but a strong shallow circulation south of 5°N was observed with strong overturning northerly flow at 850 hPa (Fig. 11b). The shallow circulation associated with the shallow convection was likely inhibited from transitioning to deep convection due to the dry mid- and upper-level conditions imposed by the nonconvectively active

part of the EW (Fig. 11d). The climatological ITCZ axis (8°N) was dominated by a negative tendency due to vertical advection and deep convection was also suppressed (Fig. 11f). However, horizontal advection anomalies were positive south of 5°N and likely helped maintain the shallow convection at day +2 (Fig. 8h). The strong northerly shallow overturning flow at 850 hPa was part of the EW horizontal structure that showed an anticyclonic circulation with strong northerly flow at day +2 (Fig. 11f). The anticyclonic circulation was vertically tilted, with northerly flow at 850 hPa (600 hPa) that reached the OTREC box at day +2 (+3) as shown in Fig. 6. Additionally, the difference between vertical advection and precipitation suggests that this region was dominated by shallow structures that produced weak precipitation (i.e., shallow cumulus and stratocumulus clouds) but relatively strong low-level convergence at days +2 and +3 (Figs. 8h and 9i,j).

To show the consistency of the three EWs in modifying the climatological deep and shallow circulations in the east Pacific ITCZ, Fig. 12 compares the meridional wind profile of each wave at days 0 and +2 at 4°–5°N (the shallow circulation region) and 7°–8°N (the deep circulation region) with the August–September 2019 mean profile. On day 0 at 7°–8°N (Fig. 12a), a deep circulation with southerly winds at low levels and northerly winds at upper levels was consistently produced across the three EWs. The deep circulations during the passage of EWs were stronger compared to the August-September average, especially during EW 1 and 2 with stronger low-level inflow. On day 0 at 4°–5°N (Fig. 12c), there was weaker overturning flow near 800 hPa in the EWs compared to the August–September profile. At day +2, the deep circulation was weaker at 7°–8°N (Fig. 12b), but the overturning flow around 800 hPa at 4°–5°N was stronger after the passage of the EWs compared to the August–September profile (Fig. 12d).

6. Summary and conclusions

This study aimed to identify synoptic variability associated with EWs during the OTREC field campaign, and determine their impacts on the climatological deep and shallow circulations in the east Pacific. Using OTREC observations, ERA5, and satellite precipitation estimates, we identified three strong EWs. Although this study considers a limited number of EW events, it analyzes a period strongly constrained by in situ observations, and the midlevel vorticity and meridional wind structures examined are consistent across all the events during the OTREC field campaign.

Modulation of the climatological shallow and deep circulations in the far east Pacific at longitudes near the OTREC observational area were found during the passage of EWs, which we depict as a schematic in Fig. 13. Normal conditions (Fig. 13a) represent the August–September 2019 mean (Fig. 1b), with a shallow circulation near 6°N below 850 hPa and a deep circulation at 8°N between the surface and 200 hPa. Positive low-level vorticity (i.e., cyclonic circulation) is also characteristic of climatological conditions (Raymond et al. 2014), with associated surface westerly winds at 7°N. Easterly winds occur near the equator between 700 and 600 hPa.

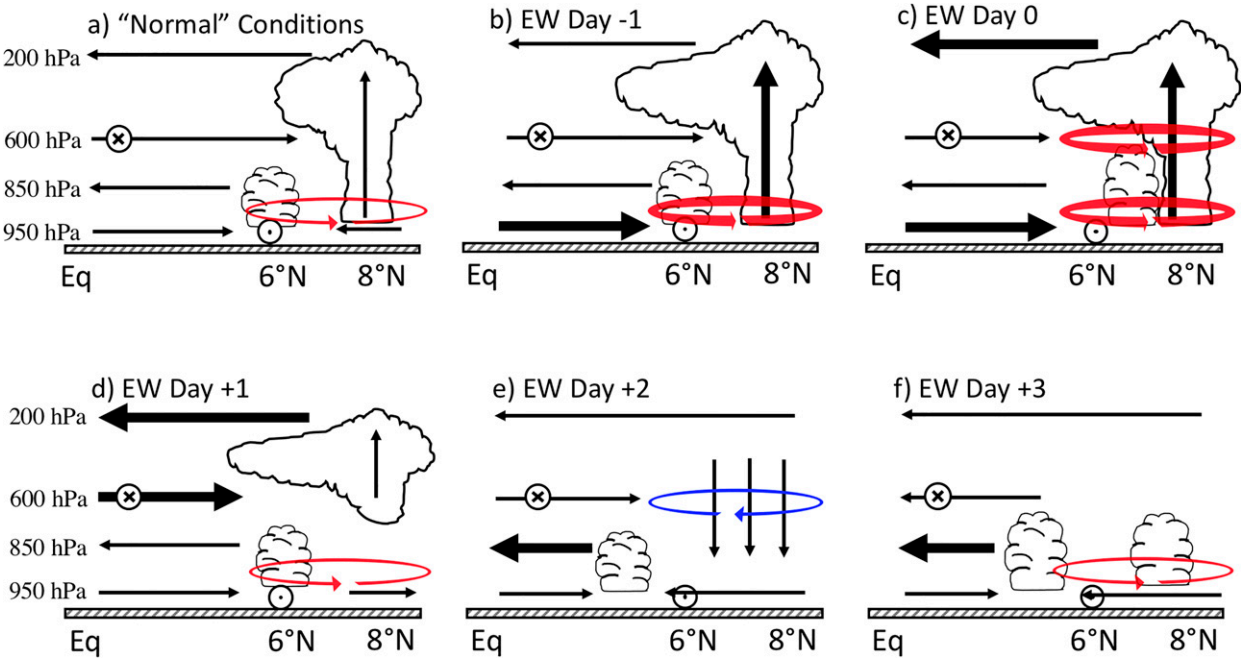

FIG. 13. Latitude–height sketch of the evolution of EWs and their effect on shallow and deep circulations in the east Pacific. Horizontal (vertical) bold vectors indicate total meridional winds (upward motion) larger than 8 m s^{-1} (0.3 Pa s^{-1}). Positive (negative) total vorticity is shown in a red cyclonic (blue anticyclonic) vertical vorticity features, and bold trajectories indicate vorticity of magnitude larger than 4×10^{-5} s^{-1}. The EW horizontal scale is approximated by the size of vorticity features. The clouds denote the position of the shallow and deep convection. Encircled × symbols (dots) denote westward (eastward) winds.

The EWs during OTREC strongly modulated these seasonal mean conditions. At day −1 of the EW evolution (Fig. 13b), deep convection was enhanced at 8°N and the total low-level positive vorticity (Fig. 6a) was stronger than climatology and associated with intensified near-surface westerly flow. At day 0 (Fig. 13c), the trough of the EW was associated with enhanced deep convection at 8°N and the shallow convection was displaced north of 6°N. This alteration is associated with the export of column integrated MSE by vertical advection. Positive vorticity predominated near the surface and at 600 hPa in the region of deep convection, associated with intensifying near-surface westerly flow just to the south of the deep convective region. At day +1 after the passage of the trough (Fig. 13d), deep convection decayed and stratiform clouds predominated at 8°N, with the net effect of vertical moisture advection and precipitation producing drying. Enhanced midlevel southerly inflow associated with the EW structure (Figs. 5g,j) and upper-level northerly outflow also occurred. At day +2 (Fig. 13e), positive values of moisture and MSE fields supported by horizontal advection in the EW ridge likely enhances shallow convection at 4°N. The strong shallow overturning circulation at 850 hPa was coupled with an EW anticyclonic structure that drove strong northerly winds between 700 and 800 hPa (Figs. 6g and 11f). At day +3 (Fig. 13f), weak convection was observed at 8°N, although the positive low-level vorticity recovered. The shallow circulation was still prominent associated with deeper and stronger shallow convection.

This schematic is consistent with the climatological deep and shallow circulations being modified by the passage of EWs in the east Pacific. The troughs of EWs enhanced the ITCZ deep circulation at day 0 and was associated with an export of column integrated MSE by vertical advection; however, the shallow circulation in the southern part of the ITCZ was weak due to a negative moisture tendency from horizontal advection over the southern part of the ITCZ. On the other hand, the suppressed part of the EW enhanced the shallow circulation at day +2. The shallow overturning flow at 850 hPa was linked to the anticyclonic circulation of the EW. A positive anomalous moisture tendency that resulted from horizontal advection and import of MSE helped drive shallow convection over the southern part of the ITCZ. This MSE import was consistent with moistening by vertical advection that outpaced precipitation, which is suggestive of an enhancement of shallow convection that fostered column moistening at day +3. Our results indicate that the three EWs altered the east Pacific ITCZ circulation in this way consistently. Even though ERA5 did not assimilate OTREC data during all the EWs, it appears capable of capturing the salient structures and variations of the EWs during this time. Future work will involve the identification of EWs during a longer time period using satellite precipitation and reanalyses to confirm the systematic alteration of the shallow and deep circulation during the passage of EWs in the east Pacific ITCZ.

Acknowledgments. The authors thank Z. Fuchs, D. Raymond, and the rest of the OTREC team for interesting discussions that improved this study. We also thank the reviewers for their constructive comments that helped to improve this manuscript. This work has been supported by NASA Earth and Space Science Fellowship (NESSF) under Grant 80NSSC18K1402P00001. EDM was supported by NSF Climate and Large-Scale Dynamics Grant AGS-1735978 and by NASA CYGNSS Grant NNX17AH77G.

REFERENCES

Back, L. E., and C. S. Bretherton, 2006: Geographic variability in the export of moist static energy and vertical motion profiles in the tropical Pacific. *Geophys. Res. Lett.*, **33**, L17810, https://doi.org/10.1029/2006GL026672.

——, and ——, 2009: On the relationship between SST gradients, boundary layer winds, and convergence over the tropical oceans. *J. Climate*, **22**, 4182–4196, https://doi.org/10.1175/2009JCLI2392.1.

Berry, G., C. Thorncroft, and T. Hewson, 2007: African easterly waves during 2004—Analysis using objective techniques. *Mon. Wea. Rev.*, **135**, 1251–1267, https://doi.org/10.1175/MWR3343.1.

Dominguez, C., J. M. Done, and C. L. Bruyère, 2020: Easterly wave contributions to seasonal rainfall over the tropical Americas in observations and a regional climate model. *Climate Dyn.*, **54**, 191–209, https://doi.org/10.1007/s00382-019-04996-7.

Frank, W. M., and P. E. Roundy, 2006: The role of tropical waves in tropical cyclogenesis. *Mon. Wea. Rev.*, **134**, 2397–2417, https://doi.org/10.1175/MWR3204.1.

Fuchs-Stone, Ž., D. J. Raymond, and S. Sentić, 2020: OTREC2019: Convection over the east Pacific and southwest Caribbean. *Geophys. Res. Lett.*, **47**, e2020GL087564, https://doi.org/10.1029/2020GL087564.

Gomes, H. B., T. Ambrizzi, B. F. Pontes da Silva, K. Hodges, P. L. Silva Dias, D. L. Herdies, M. C. L. Silva, and H. B. Gomes, 2019: Climatology of easterly wave disturbances over the tropical South Atlantic. *Climate Dyn.*, **53**, 1393–1411, https://doi.org/10.1007/s00382-019-04667-7.

Handlos, Z. J., and L. E. Back, 2014: Estimating vertical motion profile shape within tropical weather states over the oceans. *J. Climate*, **27**, 7667–7686, https://doi.org/10.1175/JCLI-D-13-00602.1.

Hersbach, H., and D. Dee, 2016: ERA5 reanalysis is in production. *ECMWF Newsletter*, No. 147, ECMWF, Reading, United Kingdom, 7, http://www.ecmwf.int/sites/default/files/elibrary/2016/16299-newsletter-no147-spring-2016.pdf.

Hodges, K., 1995: Feature tracking on the unit sphere. *Mon. Wea. Rev.*, **123**, 3458–3465, https://doi.org/10.1175/1520-0493(1995)123<3458:FTOTUS>2.0.CO;2.

——, 1999: Adaptive constraints for feature tracking. *Mon. Wea. Rev.*, **127**, 1362–1373, https://doi.org/10.1175/1520-0493(1999)127<1362:ACFFT>2.0.CO;2.

Holloway, C. E., and J. D. Neelin, 2009: Moisture vertical structure, column water vapor, and tropical deep convection. *J. Atmos. Sci.*, **66**, 1665–1683, https://doi.org/10.1175/2008JAS2806.1.

Hou, A. Y., and Coauthors, 2014: The Global Precipitation Measurement mission. *Bull. Amer. Meteor. Soc.*, **95**, 701–722, https://doi.org/10.1175/BAMS-D-13-00164.1.

Huaman, L., and K. Takahashi, 2016: The vertical structure of the eastern Pacific ITCZs and associated circulation using the TRMM Precipitation Radar and in situ data. *Geophys. Res. Lett.*, **43**, 8230–8239, https://doi.org/10.1002/2016GL068835.

——, and C. Schumacher, 2018: Assessing the vertical latent heating structure of the east Pacific ITCZ using the *CloudSat* CPR and TRMM PR. *J. Climate*, **31**, 2563–2577, https://doi.org/10.1175/JCLI-D-17-0590.1.

——, ——, and G. N. Kiladis, 2020: Eastward propagating disturbances in the tropical Pacific. *Mon. Wea. Rev.*, **148**, 3713–3728, https://doi.org/10.1175/MWR-D-20-0029.1.

Huffman, G. J., D. T. Bolvin, D. Braithwaite, K. Hsu, R. Joyce, P. Xie, and S.-H. Yoo, 2015: NASA Global Precipitation Measurement (GPM) Integrated Multi-Satellite Retrievals for GPM (IMERG). NASA Algorithm Theoretical Basis Doc., version 4, 26 pp.

Inoue, K., and L. Back, 2015: Column-integrated moist static energy budget analysis on various time scales during TOGA COARE. *J. Atmos. Sci.*, **72**, 1856–1871, https://doi.org/10.1175/JAS-D-14-0249.1.

Janiga, M. A., and C. D. Thorncroft, 2013: Regional differences in the kinematic and thermodynamic structure of African easterly waves. *Quart. J. Roy. Meteor. Soc.*, **139**, 1598–1614, https://doi.org/10.1002/qj.2047.

Jaramillo, L., G. Poveda, and J. F. Mejía, 2017: Mesoscale convective systems and other precipitation features over the tropical Americas and surrounding seas as seen by TRMM. *Int. J. Climatol.*, **37**, 380–397, https://doi.org/10.1002/joc.5009.

Kiladis, G. N., C. D. Thorncroft, and N. M. Hall, 2006: Three-dimensional structure and dynamics of African easterly waves. Part I: Observations. *J. Atmos. Sci.*, **63**, 2212–2230, https://doi.org/10.1175/JAS3741.1.

——, M. C. Wheeler, P. T. Haertel, K. H. Straub, and P. E. Roundy, 2009: Convectively coupled equatorial waves. *Rev. Geophys.*, **47**, RG2003, https://doi.org/10.1029/2008RG000266.

Lindzen, R. S., and S. Nigam, 1987: On the role of sea surface temperature gradients in forcing low-level winds and convergence in the tropics. *J. Atmos. Sci.*, **44**, 2418–2436, https://doi.org/10.1175/1520-0469(1987)044<2418:OTROSS>2.0.CO;2.

Martin, E. R., and C. Schumacher, 2011: Modulation of Caribbean precipitation by the Madden–Julian oscillation. *J. Climate*, **24**, 813–824, https://doi.org/10.1175/2010JCLI3773.1.

Masunaga, H., and Z. J. Luo, 2016: Convective and large-scale mass flux profiles over tropical oceans determined from synergistic analysis of a suite of satellite observations. *J. Geophys. Res. Atmos.*, **121**, 7958–7974, https://doi.org/10.1002/2016JD024753.

Molinari, J., and D. Vollaro, 2000: Planetary-and synoptic-scale influences on eastern Pacific tropical cyclogenesis. *Mon. Wea. Rev.*, **128**, 3296–3307, https://doi.org/10.1175/1520-0493(2000)128<3296:PASIO>2.0.CO;2.

——, D. Knight, M. Dickinson, D. Vollaro, and S. Skubis, 1997: Potential vorticity, easterly waves, and eastern Pacific tropical cyclogenesis. *Mon. Wea. Rev.*, **125**, 2699–2708, https://doi.org/10.1175/1520-0493(1997)125<2699:PVEWAE>2.0.CO;2.

Nolan, D. S., and E. D. Rappin, 2008: Increased sensitivity of tropical cyclogenesis to wind shear in higher SST environments. *Geophys. Res. Lett.*, **35**, L14805, https://doi.org/10.1029/2008GL034147.

——, C. Zhang, and S. Chen, 2007: Dynamics of the shallow meridional circulation around intertropical convergence zones. *J. Atmos. Sci.*, **64**, 2262–2285, https://doi.org/10.1175/JAS3964.1.

——, S. W. Powell, C. Zhang, and B. E. Mapes, 2010: Idealized simulations of the intertropical convergence zone and its multilevel flows. *J. Atmos. Sci.*, **67**, 4028–4053, https://doi.org/10.1175/2010JAS3417.1.

Pasch, R. J., and Coauthors, 2009: Eastern North Pacific hurricane season of 2006. *Mon. Wea. Rev.*, **137**, 3–20, https://doi.org/10.1175/2008MWR2508.1.

Petersen, W. A., R. Cifelli, D. J. Boccippio, S. A. Rutledge, and C. Fairall, 2003: Convection and easterly wave structures observed in the eastern Pacific warm pool during EPIC-2001. *J. Atmos. Sci.*, **60**, 1754–1773, https://doi.org/10.1175/1520-0469(2003)060<1754:CAEWSO>2.0.CO;2.

Poveda, G., L. Jaramillo, and L. F. Vallejo, 2014: Seasonal precipitation patterns along pathways of South America low-level jets and aerial rivers. *Water Resour. Res.*, **50**, 98–118, https://doi.org/10.1002/2013WR014087.

Rapp, A. D., A. G. Peterson, O. W. Frauenfeld, S. M. Quiring, and E. B. Roark, 2014: Climatology of storm characteristics in Costa Rica using the TRMM Precipitation Radar. *J. Hydrometeor.*, **15**, 2615–2633, https://doi.org/10.1175/JHM-D-13-0174.1.

Rauber, R. M., S. M. Ellis, J. Vivekanandan, J. Stith, W.-C. Lee, G. M. McFarquhar, B. F. Jewett, and A. Janiszeski, 2017: Finescale structure of a snowstorm over the northeastern United States: A first look at high-resolution HIAPER Cloud Radar observations. *Bull. Amer. Meteor. Soc.*, **98**, 253–269, https://doi.org/10.1175/BAMS-D-15-00180.1.

Raymond, D. J., C. López-Carrillo, and L. L. Cavazos, 1998: Case-studies of developing east Pacific easterly waves. *Quart. J. Roy. Meteor. Soc.*, **124**, 2005–2034, https://doi.org/10.1002/qj.49712455011.

——, S. Gjorgjievska, S. Sessions, and Z. Fuchs, 2014: Tropical cyclogenesis and mid-level vorticity. *Aust. Meteor. Oceanogr. J.*, **64**, 11–25, https://doi.org/10.22499/2.6401.003.

Reed, R. J., and E. E. Recker, 1971: Structure and properties of synoptic-scale wave disturbances in the equatorial western Pacific. *J. Atmos. Sci.*, **28**, 1117–1133, https://doi.org/10.1175/1520-0469(1971)028<1117:SAPOSS>2.0.CO;2.

——, and R. H. Johnson, 1974: The vorticity budget of synoptic-scale wave disturbances in the tropical western Pacific. *J. Atmos. Sci.*, **31**, 1784–1790, https://doi.org/10.1175/1520-0469(1974)031<1784:TVBOSS>2.0.CO;2.

——, D. C. Norquist, and E. E. Recker, 1977: The structure and properties of African wave disturbances as observed during phase III of GATE. *Mon. Wea. Rev.*, **105**, 317–333, https://doi.org/10.1175/1520-0493(1977)105<0317:TSAPOA>2.0.CO;2.

Rennick, M. A., 1976: The generation of African waves. *J. Atmos. Sci.*, **33**, 1955–1969, https://doi.org/10.1175/1520-0469(1976)033<1955:TGOAW>2.0.CO;2.

Riehl, H., 1954: *Tropical Meteorology*. McGraw-Hill, 392 pp.

Rydbeck, A. V., and E. D. Maloney, 2014: Energetics of east Pacific easterly waves during intraseasonal events. *J. Climate*, **27**, 7603–7621, https://doi.org/10.1175/JCLI-D-14-00211.1.

——, and ——, 2015: On the convective coupling and moisture organization of east Pacific easterly waves. *J. Atmos. Sci.*, **72**, 3850–3870, https://doi.org/10.1175/JAS-D-15-0056.1.

——, ——, and G. J. Alaka Jr., 2017: In situ initiation of east Pacific easterly waves in a regional model. *J. Atmos. Sci.*, **74**, 333–351, https://doi.org/10.1175/JAS-D-16-0124.1.

Schumacher, C., R. A. Houze Jr., and I. Kraucunas, 2004: The tropical dynamical response to latent heating estimates derived from the TRMM Precipitation Radar. *J. Atmos. Sci.*, **61**, 1341–1358, https://doi.org/10.1175/1520-0469(2004)061<1341:TTDRTL>2.0.CO;2.

Serra, Y. L., and , R. A. Houze Jr., 2002: Observations of variability on synoptic timescales in the east Pacific ITCZ. *J. Atmos. Sci.*, **59**, 1723–1743, https://doi.org/10.1175/1520-0469(2002)059<1723:OOVOST>2.0.CO;2.

——, G. N. Kiladis, and M. F. Cronin, 2008: Horizontal and vertical structure of easterly waves in the Pacific ITCZ. *J. Atmos. Sci.*, **65**, 1266–1284, https://doi.org/10.1175/2007JAS2341.1.

——, ——, and K. I. Hodges, 2010: Tracking and mean structure of easterly waves over the Intra-Americas Sea. *J. Climate*, **23**, 4823–4840, https://doi.org/10.1175/2010JCLI3223.1.

——, X. Jiang, B. Tian, J. Amador-Astua, E. D. Maloney, and G. N. Kiladis, 2014: Tropical intraseasonal modes of the atmosphere. *Annu. Rev. Environ. Resour.*, **39**, 189–215, https://doi.org/10.1146/annurev-environ-020413-134219.

Shapiro, L. J., 1986: The three-dimensional structure of synoptic-scale disturbances over the tropical Atlantic. *Mon. Wea. Rev.*, **114**, 1876–1891, https://doi.org/10.1175/1520-0493(1986)114<1876:TTDSOS>2.0.CO;2.

Sherwood, S. C., P. Minnis, and M. McGill, 2004: Deep convective cloud-top heights and their thermodynamic control during CRYSTAL-FACE. *J. Geophys. Res.*, **109**, D20119, https://doi.org/10.1029/2004JD004811.

Tai, K.-S., and Y. Ogura, 1987: An observational study of easterly waves over the eastern Pacific in the northern summer using FGGE data. *J. Atmos. Sci.*, **44**, 339–361, https://doi.org/10.1175/1520-0469(1987)044<0339:AOSOEW>2.0.CO;2.

Thompson, R. M., S. W. Payne, E. E. Recker, and R. J. Reed, 1979: Structure and properties of synoptic-scale wave disturbances in the intertropical convergence zone of the eastern Atlantic. *J. Atmos. Sci.*, **36**, 53–72, https://doi.org/10.1175/1520-0469(1979)036<0053:SAPOSS>2.0.CO;2.

Thorncroft, C., and B. Hoskins, 1994: An idealized study of African easterly waves. I: A linear view. *Quart. J. Roy. Meteor. Soc.*, **120**, 953–982, https://doi.org/10.1002/qj.49712051809.

Toma, V. E., and P. J. Webster, 2010a: Oscillations of the intertropical convergence zone and the genesis of easterly waves. Part I: Diagnostics and theory. *Climate Dyn.*, **34**, 587–604, https://doi.org/10.1007/s00382-009-0584-x.

——, and ——, 2010b: Oscillations of the intertropical convergence zone and the genesis of easterly waves. Part II: Numerical verification. *Climate Dyn.*, **34**, 605–613, https://doi.org/10.1007/s00382-009-0585-9.

Vömel, H., and Coauthors, 2021: High-resolution in situ observations of atmospheric thermodynamics using dropsondes during the Organization of Tropical East Pacific Convection (OTREC) field campaign. *Earth Syst. Sci. Data*, **13**, 1107–1117, https://doi.org/10.5194/essd-13-1107-2021.

Whitaker, J. W., and E. D. Maloney, 2018: Influence of the Madden–Julian oscillation and Caribbean low-level jet on east Pacific easterly wave dynamics. *J. Atmos. Sci.*, **75**, 1121–1141, https://doi.org/10.1175/JAS-D-17-0250.1.

——, and ——, 2020: Genesis of an east Pacific easterly wave from a Panama Bight MCS: A case study analysis from June 2012. *J. Atmos. Sci.*, **77**, 3567–3584, https://doi.org/10.1175/JAS-D-20-0032.1.

Wolding, B. O., and E. D. Maloney, 2015: Objective diagnostics and the Madden–Julian oscillation. Part II: Application to moist static energy and moisture budgets. *J. Climate*, **28**, 7786–7808, https://doi.org/10.1175/JCLI-D-14-00689.1.

——, ——, and M. Branson, 2016: Vertically resolved weak temperature gradient analysis of the Madden–Julian oscillation in SP-CESM. *J. Adv. Model. Earth Syst.*, **8**, 1586–1619, https://doi.org/10.1002/2016MS000724.

Xie, S.-P., H. Xu, W. S. Kessler, and M. Nonaka, 2005: Air–sea interaction over the eastern Pacific warm pool: Gap winds, thermocline dome, and atmospheric convection. *J. Climate*, **18**, 5–20, https://doi.org/10.1175/JCLI-3249.1.

Ye, B., A. D. Del Genio, and K. K. Lo, 1998: Cape variations in the current climate and in a climate change. *J. Climate*, **11**, 1997–2015, https://doi.org/10.1175/1520-0442-11.8.1997.

Yokoyama, C., and Y. N. Takayabu, 2012: Relationships between rain characteristics and environment. Part II: Atmospheric disturbances associated with shallow convection over the eastern tropical Pacific. *Mon. Wea. Rev.*, **140**, 2841–2859, https://doi.org/10.1175/MWR-D-11-00251.1.

Zehnder, J. A., D. M. Powell, and D. L. Ropp, 1999: The interaction of easterly waves, orography, and the intertropical convergence zone in the genesis of eastern Pacific tropical cyclones. *Mon. Wea. Rev.*, **127**, 1566–1585, https://doi.org/10.1175/1520-0493(1999)127<1566:TIOEWO>2.0.CO;2.

Zhang, C., M. McGauley, and N. A. Bond, 2004: Shallow meridional circulation in the tropical eastern Pacific. *J. Climate*, **17**, 133–139, https://doi.org/10.1175/1520-0442(2004)017<0133:SMCITT>2.0.CO;2.

——, D. S. Nolan, C. D. Thorncroft, and H. Nguyen, 2008: Shallow meridional circulations in the tropical atmosphere. *J. Climate*, **21**, 3453–3470, https://doi.org/10.1175/2007JCLI1870.1.

Zuidema, P., B. Mapes, J. Lin, C. Fairall, and G. Wick, 2006: The interaction of clouds and dry air in the eastern tropical Pacific. *J. Climate*, **19**, 4531–4544, https://doi.org/10.1175/JCLI3836.1.